学位論文

Study of biogenic calcite regulated by intracrystalline organic molecules
(結晶内有機分子に制御された生物起源カルサイトに関する研究)

平成２５年１２月博士（理学）申請

東京大学大学院理学系研究科

地球惑星科学専攻

奥村　大河

Abstract

Biogenic mineralized tissues, or biominerals, contain not only inorganic constituents but also organic phases, which contributes to their superior properties to geological minerals. Such biominerals as organic–inorganic composites have been attracting a lot of attention because of their potential applications to functional materials over the decades. The organic phases in biominerals can be classified into *inter*crystalline and *intra*crystalline organic molecules (abbreviated as OMs in this study), both of which play important roles in biomineralization processes. Compared with the intercrystalline OMs, the intracrystalline OMs have been rarely investigated owing to the difficulty of dealing with them. In the preset study, I show that intracrystalline OMs induce defect-rich microstructures in calcite crystals constituting outer layers of mollusk shells, mainly by using recent electron microscopic techniques. Compared to geological calcite which readily cleaves owing to its intrinsic crystal structure, biogenic calcite overcomes this mechanical weakness by occluding OMs inside crystals. Elaborate interaction between crystals and intracrystalline OMs invests the distinctive characters of biogenic calcite.

First, the prismatic structures of two bivalve shells, *Pinctada fucata* and *Atrina pectinata*, were crystallographically inquired. Scanning electron microscopy (SEM) observation revealed the existence of membranous and net-like OMs, which are insoluble in ethylenediaminetetraacetic acid (EDTA), inside the prisms of *Pinctada*. The insoluble OMs were observed as bright Fresnel contrasts in under-focused transmission electron microscopy (TEM) images, which were confirmed as organic phase by electron energy-loss spectroscopy. Defect-rich sub-grain structures with small-angle misorientation are induced by the insoluble OMs, which probably results in gradual

orientation change over the crystals, as observed by electron back-scatter diffraction (EBSD) in SEM in my previous study. The membranous and net like distribution of the intracrystalline OMs in the prismatic crystals was also confirmed by scanning TEM (STEM) tomography with high-angle annular dark-field (HAADF) imaging. X-ray diffraction measurements demonstrated that great local lattice strain is induced by the defect-rich structure. In contrast, the insoluble OMs in *Atrina* are shaped like thin fibers and do not influence the crystal structure. Consequently the calcite crystal of *Atrina* exhibits a defect-free single-crystalline feature.

I also analyzed the calcite crystals in the outer layers of other bivalve (*Pteria penguin* and *Crassostrea nippona*) and gastropod shells (*Haliotis discus hannai* and *Collisella dorsuosa*). These bivalve and gastropod shells have a defect-rich structure generated by reticulated OMs as observed in *Pinctada*, suggesting that such a microstructure is common among the calcite crystals in the outer layers of the mollusk shells. Nanoindentation tests indicated that the defective microstructure contributes to inhibiting the propagation of cleavages along {104} planes of calcite, implying that diverse mollusks improve the mechanical strength of their shells owing to the defect-rich structure.

Next, I examined the influence of intracrystalline OMs on crystal microstructure of calcite, via synthetic experiments. Calcite crystals were synthesized *in vitro* in the presence of OMs extracted by EDTA from the prisms of *Pinctada* and *Atrina*. The resulting crystals containing the EDTA-soluble OMs from *Pinctada* displayed a defective structure, whereas the crystals contain few defects in the case of the OMs extracted from *Atrina*. These results are comparable with the characters of actual shell structures. Therefore it is concluded that not only reticulate and EDTA-insoluble OMs

but also EDTA-soluble OMs participate in forming the microstructure of the calcite shells.

On the basis of these results, I propose the following mechanism by which intracrystalline OMs regulate the microstructure of calcite crystals constituting outer layers of mollusk shells (Abstract Figure).

1. An organic framework is constructed by OMs which include intercrystalline OMs and subsequent intracrystalline OMs with thin reticulate form. Another kind of OMs soluble in EDTA binds the reticulate OMs.

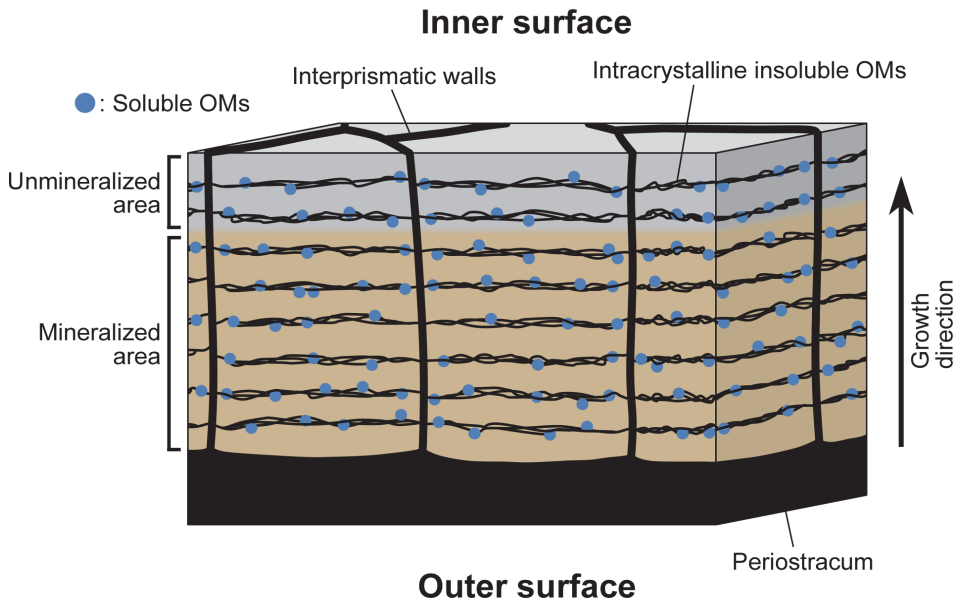

Abstract Figure. Schematic illustration of the prismatic structure, showing the mechanism by which intracrystalline OMs regulate the microstructure of calcite crystals constituting outer layers of mollusk shells.

2. As the calcite crystals interact with EDTA-soluble OMs bound to the reticulate OMs, they grow inside the intercrystalline OMs, penetrating the reticulate OMs.
3. These intracrystalline OMs are incorporated into the crystals and build sub-grain microstructures with small-angle misorientation and defect-rich boundaries, which improve the mechanical properties of biogenic calcite by inhibiting propagation of cleavages.

Contents

Chapter 1.

Introduction of this study

1.1 Overview of biomineralization

"Biomineralization" is the processes by which living organisms produce inorganic materials. Such materials are called "biominerals," but this term refers not only to the pure inorganic materials formed by organisms but also to the composite products which consist of both inorganic and organic components. More than 60 kinds of materials or minerals have been identified as biominerals to date (Table 1–1), among which calcium carbonates are the most abundant biominerals (Weiner and Addadi, 2002). As calcium carbonate minerals, five crystalline and one amorphous phases, which have the same principal composition ($CaCO_3$) with different structures, are known; calcite, aragonite, vaterite, calcium carbonate monohydrate, calcium carbonate hexahydrate and amorphous calcium carbonate (ACC). Calcite and aragonite are the most thermodynamically stable polymorphs under ambient conditions and formed extensively as biominerals. The fact that many organisms produce both calcite and aragonite simultaneously is a famous and intriguing topic as the "calcite–aragonite problem." Less stable vaterite and monohydrocalcite are formed by a limited number of organisms and calcium carbonate hexahydrate, ikaite, has not been known to be formed biologically yet. ACC is extremely unstable, but Addadi et al. (2003) reported that some organisms produce ACC either as a stable phase or as a transient precursor of more stable crystalline calcite or aragonite. Nowadays many researchers are trying to elucidate the mechanisms for stabilizing ACC in biominerals (e.g., Tao et al., 2009; Bentov et al., 2010; Sato et al., 2011).

Biomineralization is divided into two fundamentally different processes based on the relationship between mineralization and activities of organisms. One is

Table 1–1. Minerals produced by biomineralization processes. (Adapted from Weiner and Addadi, 2002; Weiner and Dove, 2003)

Carbonates	Calcite	Monohydrocalcite
	Mg-calcite	Amorphous calcium carbonate
	Aragonite	Protodolomite
	Vaterite	Hydrocerrusite
Phosphates	Carbonated-apatite	Amorphous calcium phosphate
	Octacalcium phosphate	Amorphous calcium pyrophosphate
	Francolite	Struvite
	Whitlockite	Vivianite
	Brushite	
Sulfates	Gypsum	Celestite
	Barite	Jarosite
Sulfides	Pyrite	Greigite
	Hydrotroilite	Mackinawite
	Sphalerite	Amorphous pyrrhotite
	Wurtzite	Acanthite
	Galena	
Silicates	Silica	
Fluorides	Fluorite	Hieratite
Chlorides	Atacamite	
Metals	Sulfur	
Oxides	Magnetite	Amorphous iron oxide
	Amorphous ilmenite	Amorphous manganese oxide
Hydroxides	Goethite	Todorokite
	Lepidocrocite	Birnessite
	Ferrihydrite	
“Organic minerals”	Whewellite	Uric acid
	Weddelite	Paraffin hydrocarbon
	Manganese oxalate	Calcium tartrate
	Magnesium oxalate	Calcium malate
	Copper oxalate	Earlandite
	Ferric oxalate anhydrous	Sodium urate
	Guanine	

biologically induced mineralization (BIM) and the other is organic matrix-mediated mineralization (Lowenstam, 1981) or biologically controlled mineralization (BCM) (Mann, 2001).

BIM is secondary precipitation of minerals as a result of environmental changes due to biological activities (Figure 1–1). The metabolic activities of organisms in a particular redox environment change pH, pCO_2, redox potential (E_h), etc. and minerals generally nucleate and grow extracellularly (Frankel and Bazylinski, 2003). For example, some cyanobacteria absorb bicarbonate ions from surrounding solution and release hydroxyl anions, which locally increases pH and promotes the deposition of many kinds of minerals such as gypsum, calcite, Fe and Mn oxides/oxyhydroxides, and iron sulfides (Figure 1–2; Fortin and Beveridge, 2000). Since biological systems have

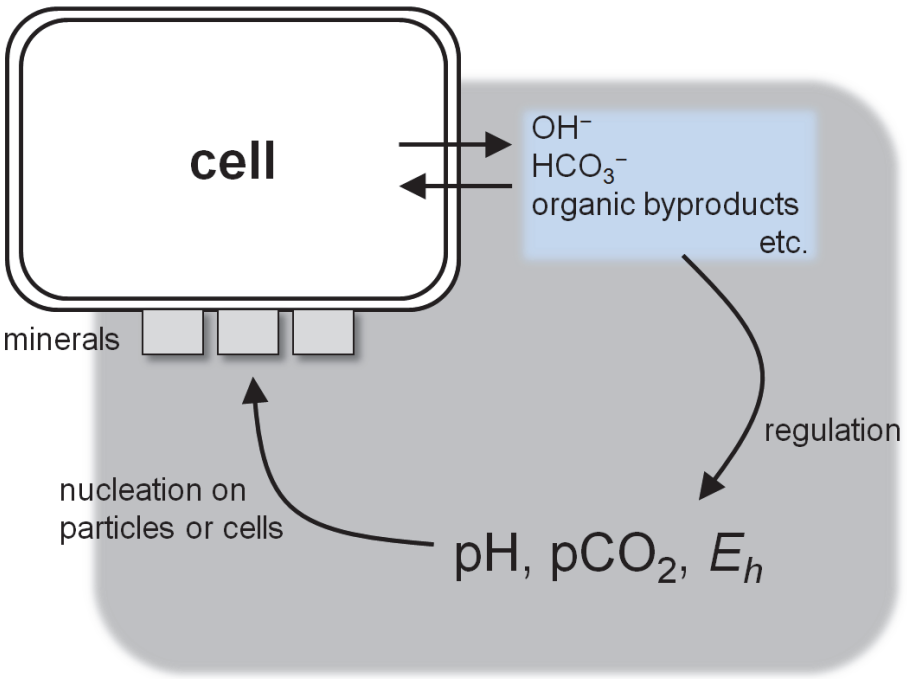

Figure 1–1. Schematic of BIM. Minerals are formed as a result of metabolic activities that regulate pH, pCO_2 and E_h.

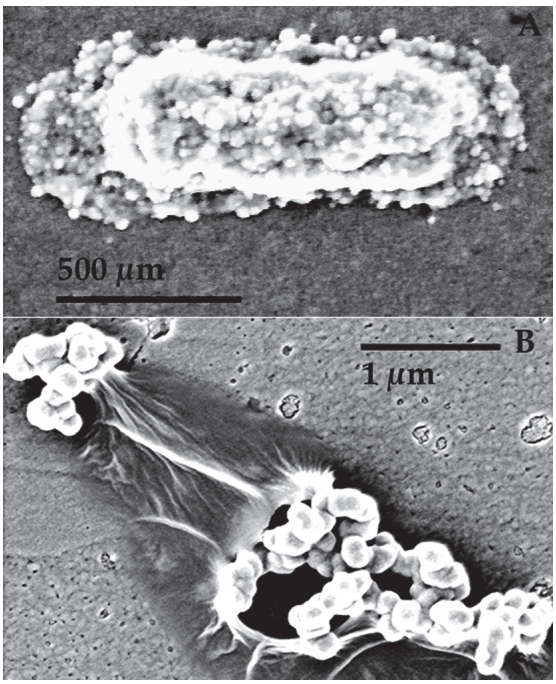

Figure 1–2. (A) SEM image of a mineralized cell of *Acidithiobacillus ferrooxidans* on pyrite. Ferric oxyhydroxide which was deposited by oxidation of pyrite covers the cell. (B) High-resolution SEM image of the ferric oxyhydroxide. (Frankel and Bazylinski, 2003).

little control over the structure and properties of the minerals deposited, BIM is almost equivalent to inorganic mineralization in the same environmental conditions. Therefore the minerals have many features that are generally indistinguishable from minerals produced by abiogenic processes.

In BCM, minerals are usually deposited on or within organic matter which regulates nucleation and growth of the minerals and influences their phases, crystal orientation, size, morphology and properties. The mineral formation is not sensitive to environmental parameters (e.g., pH, pCO_2, E_h) outside the organisms because almost all BCM processes occur in an environment isolated and regulated by organisms. Organisms often form biologically controlled minerals specialized for biological functions such as protection from enemy attacks, mechanical support for soft bodies, storage of elements, and a sensor of balance. Shells, teeth, bones and otoliths are well-known biologically controlled minerals. According to Weiner and Dove (2003),

BCM can be classified into extra-, inter- and intracellular mineralization based on the locations of mineralization sites. Each type of mineralization is described below.

In biologically controlled extracellular mineralization, frameworks are formed using organic matter such as proteins and polysaccharides, and subsequently minerals develop upon or inside the pre-formed organic frameworks (Figure 1–3). Several studies indicate that the proteins contain a lot of acidic amino acids, especially aspartic acids (Weiner, 1979). Mollusk shells, which were investigated in this study, are a typical example of the biologically controlled extracellular mineralization. For instance, Nakahara (1979) observed the nacreous layer of a gastropod shell, in which organic sheets form three-dimensional frameworks and subsequently aragonite crystals fill the spaces between the sheets (Figure 1–4).

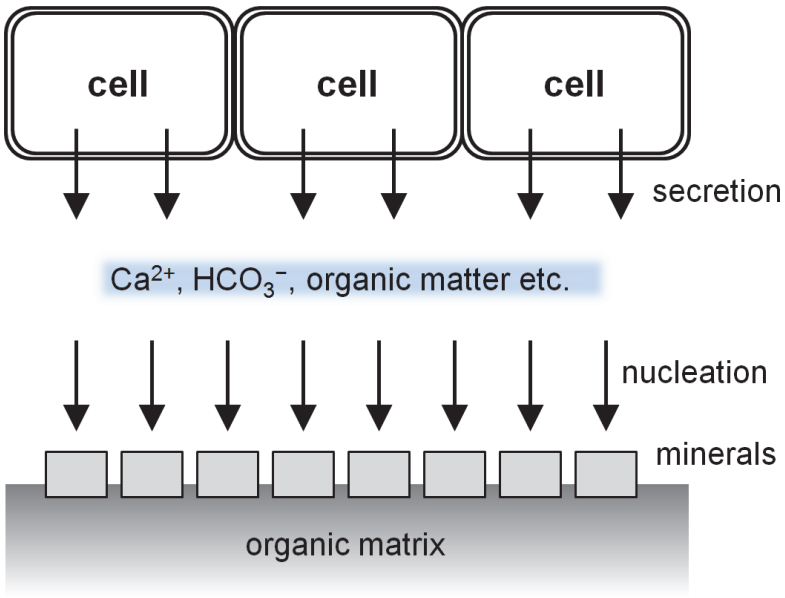

Figure 1–3. Schematic of biologically controlled extracellular mineralization. Cations and organic matter are supplied by cells and promote crystal nucleation on or inside pre-formed organic frameworks.

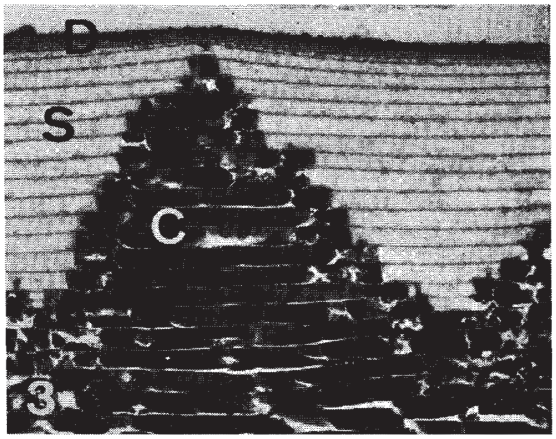

Figure 1–4. TEM image of a cross section of the nacreous layer in a gastropod shell, *Tegula pfeifferi*. Organic sheets (S) were pre-formed, and crystals (C) deposited between the sheets. (Nakahara, 1979).

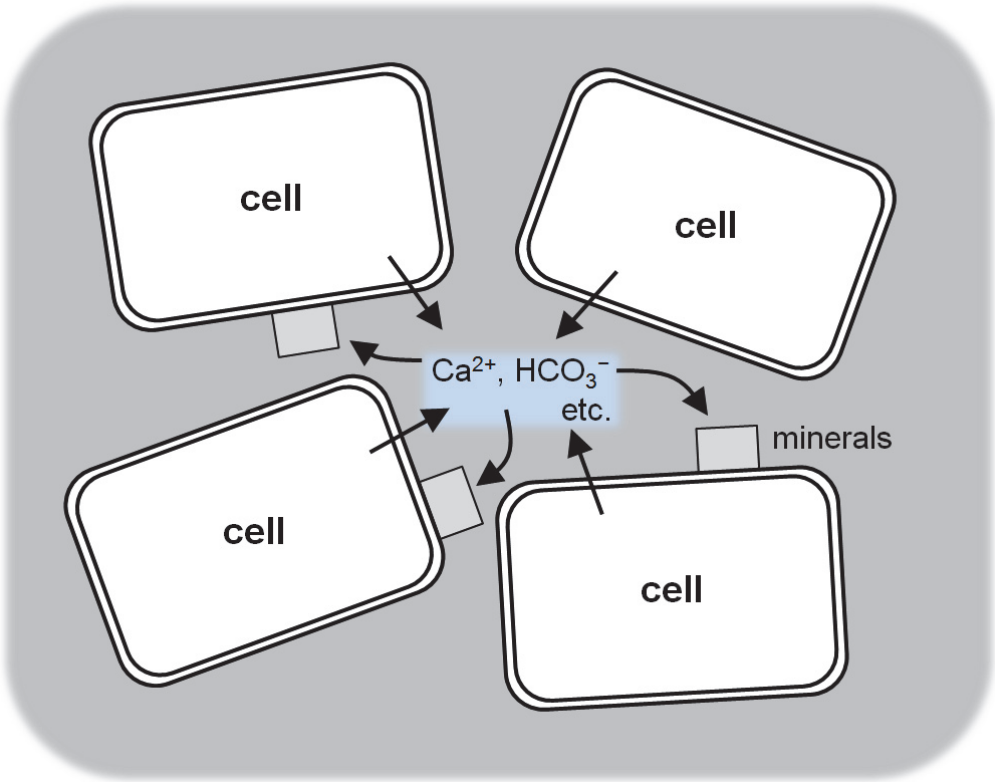

Figure 1–5. Schematic of biologically controlled intercellular mineralization. Epidermis serves as mineralization sites and controls the polymorphs, shapes and orientations of crystals.

Biologically controlled intercellular mineralization is not widespread and mainly occurs by single-cell organisms which exist as a community (Figure 1–5). This type of mineralization differs from extracellular mineralization in the way that mineralization sites are isolated by epidermis of individual organisms (Mann, 2001). It differs also from biologically induced mineralization in the way that the polymorphs, shapes and orientations of minerals are controlled by the epidermis (Borowitzka, 1982). Figure 1–6 shows an example of calcite crystals formed by algae, *Lithophyllum moluccense*. The crystals are precipitated intercellularly, but the algae regulated the *c*-axes of crystals that are perpendicular to the cell surfaces.

In biologically controlled intracellular mineralization, the environments of mineralization sites are strongly regulated by cells. In many cases, minerals are produced intracellularly and subsequently become extracellular components (Figure 1–7). A typical example is Haptophyte algae which form calcified scales called

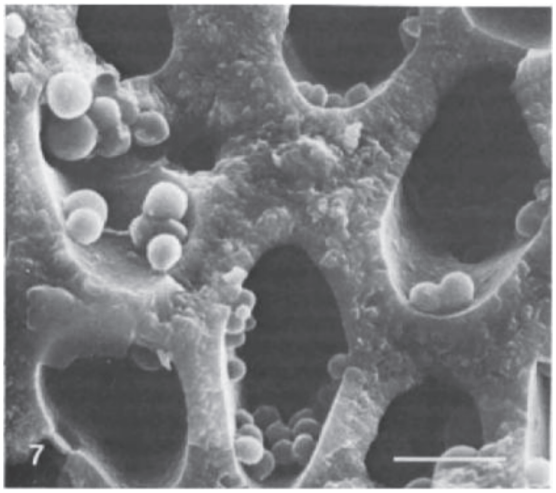

Figure 1–6. SEM image of calcite crystals attached to the cell walls of thalluses in an alga, *Lithophyllum moluccense*. The *c*-axes of calcite crystals are perpendicular to the cell surfaces. Scale bar: 5 μm. (Borowitzka, 1982).

coccoliths (Figure 1–8; Paasche, 2002). On the other hand, magnetotactic bacteria produce iron oxide nanoparticles called magnetosomes intracellularly and leave them within the cells even after mineralization (Figure 1–9; Bazylinski, 1996; Schüler and Frankel, 1999; Bazylinski and Frankel, 2003).

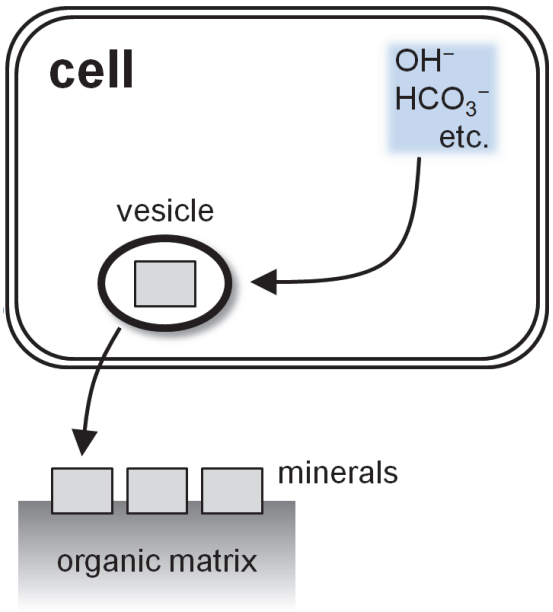

Figure 1–7. Schematic of biologically controlled intracellular mineralization. Crystals are nucleated within an intracellular environment, and subsequently secreted in many cases.

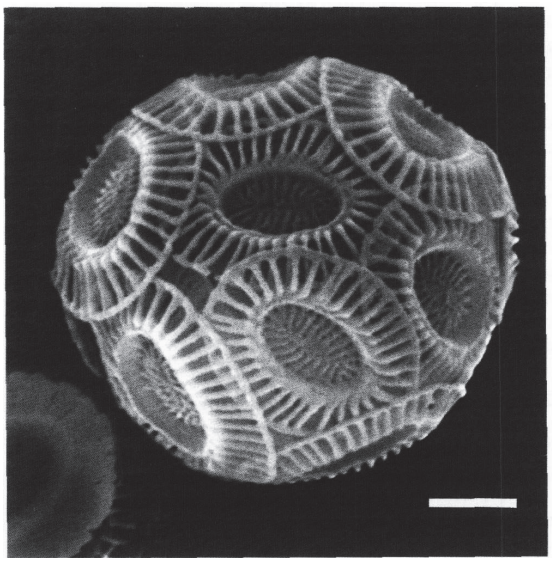

Figure 1–8. SEM image of coccoliths that are composed of calcite crystals in Haptophyte algae, *Emiliania huxleyi*. Scale bar: 1 μm. (Paasche, 2002).

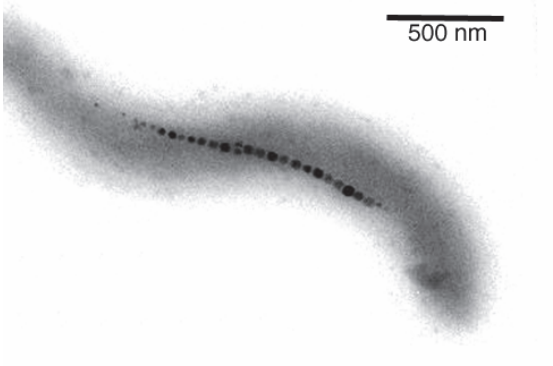

Figure 1–9. TEM image of a magnetotactic bacterium, *Magnetospirillum magnetotacticum*, with a chain of magnetite magnetosomes. (Bazylinski and Frankel, 2003).

1.2 Importance of biomineralization

Biomineralization has been studied in many areas of sciences because a lot of information is embedded in biominerals. The inorganic parts of biominerals are preserved as fossils in sediment, from which we can understand the evolution of species and the ancient environments. The large concretions called stromatolites are evidence that inorganic minerals were formed by biological activities 2.7 billion years ago (Hofmann and Masson, 1994). Thus biominerals are very important and useful clues in sedimentology, palaeontology and taxonomy to know paleoenvironments, biological evolution of metabolism and physiology. In these areas, the most common approach is identifying the taxa that faithfully preserve ancient environmental information. However, without sufficient understanding of biological or physiological effects on biomineralization, it is impossible to assess whether the fossils of taxa really preserve ancient information or not (Urey et al., 1951).

Fossils contain records not only of biological information but also of the local climate and chemical conditions of the marine environments in which organisms lived.

For example, paleotemperature of ancient seawater can be estimated from a stable oxygen isotopic composition of biominerals (Urey et al., 1951), and salinity from the amount of trace metals such as strontium (Lowenstam, 1964). More than 10 proxies for investigating different environmental parameters have been found to date. Since global climate change has recently become a big issue, understanding the details of past climate changes is necessary to assess the significance of the present change. Thus importance of paleoceanography reconstructing ancient ocean environments increases (Schrag and Linsley, 2002). However, Epstein et al. (1951) mentioned that not all biominerals are deposited in equilibrium conditions with isotopes or trace elements because of physiological effects. Consequently, deep understanding of biomineralization is required to discuss whether these proxies are trustworthy or not.

Biominerals are also a big storage of elements such as calcium, iron, carbon, phosphorus and silicon, which are cycled over millions of years through complex pathways in geosphere (Figure 1–10). The huge chalk deposits of the white cliffs on the south coast of Britain, which are made of almost only fossilized coccoliths, are a famous example (Mann, 2001). The fluxes in elemental cycles are affected by not only generation but also dissolution of biominerals (Van Cappellen, 2003).

In addition to basic research of biomineralization, its concepts are inspiring applied research such as materials science, or biomimetics (Mann, 1993; Cölfen and Mann, 2003). As stated above, many biominerals are composed of organic–inorganic composites with highly regulated structures, and perform important functions in biological activities, which include protection (Franceschi and Nakata, 2005); cutting and grinding (Wang et al., 1997); optical, magnetic and gravity sensing (Mann et al., 1983; Dunin-Borkowski et al., 1998; Aizenberg et al., 2001); and storage (Luquet and

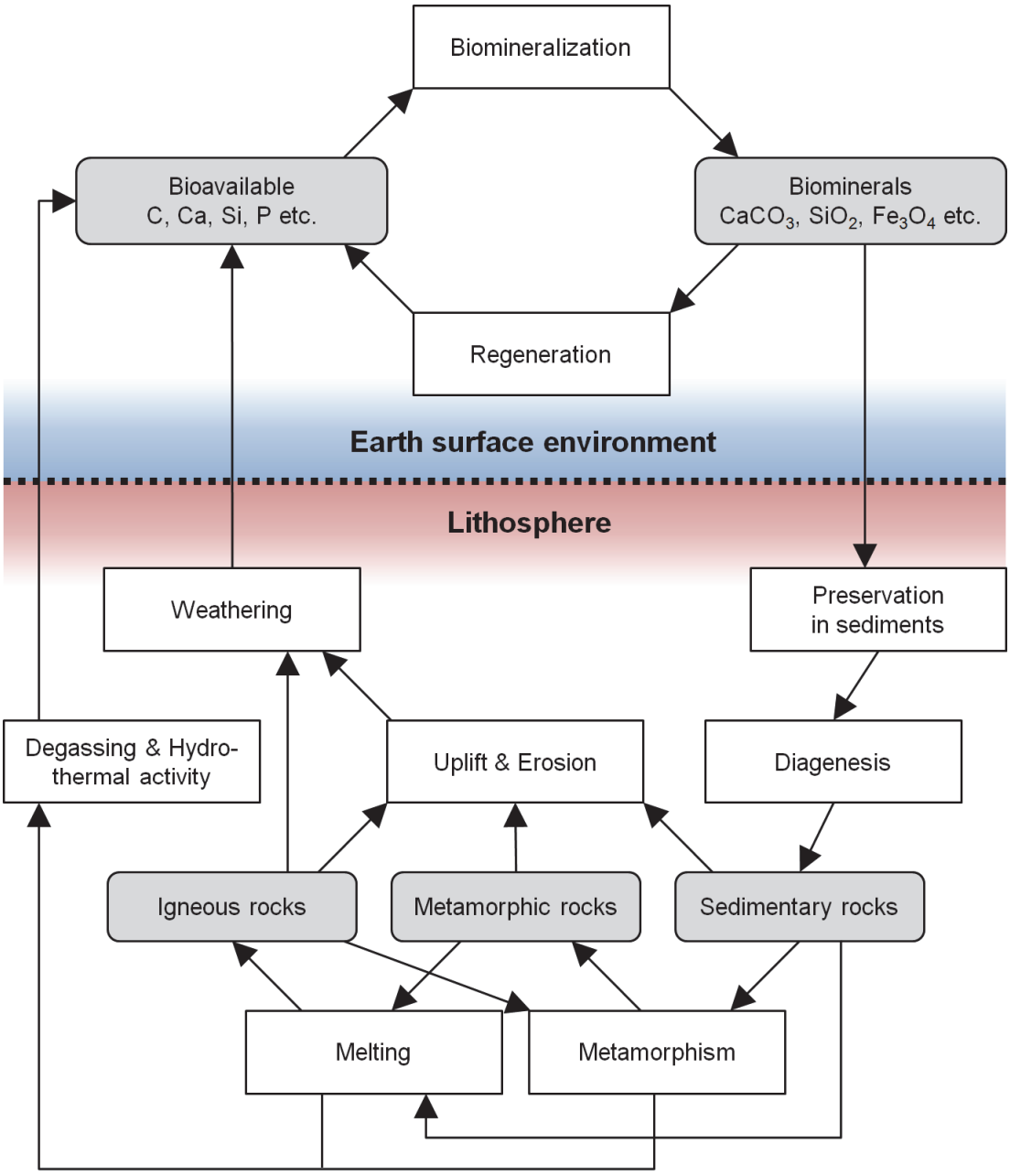

Figure 1–10. Biomineralization in elemental cycles. (Adapted from Van Cappellen, 2003).

Marin, 2004). Therefore they are attracting a lot of attention as functional materials that can be produced at ambient temperatures and pressures (Meldrum, 2003; Song and Cölfen, 2011). For instance, organic–inorganic composites of biominerals are ideal strong and tough materials. Although tough materials can be made only from organic matter such as α-chitin in insect cuticle, a great deal of energy is consumed to form such organic building blocks in organisms (Palmer, 1992). Furthermore, organic materials are tough but soft. On the other hand, inorganic materials are hard and stiff but brittle. In biominerals, organic materials construct frameworks and inorganic ones fill the spaces, which realizes organic–inorganic hybrid materials with excellent mechanical properties using less energy.

In the present study, I investigated mollusk shells, which are widely distributed throughout the world and have been paid a lot of attention among various biominerals. Many studies have been conducted for the purpose of revealing the structures, properties, and relationships between them in mollusk shells. The shells basically consist of calcium carbonate crystals combined with organic matter. Generally, mollusks use only two major phases of calcium carbonate, calcite and aragonite, which organize multiple layers in the shell structures. The organic matter constitutes frameworks in an extrapallial fluid secreted by mantle cells, and subsequently inorganic crystals nucleate on them, according to the scheme of biologically controlled extracellular mineralization as mentioned above (Addadi et al., 2006; Nudelman et al., 2006).

Mollusk shells have been investigated by a lot of researchers in various fields. Compared with abiogenic crystals, the shells have superior mechanical properties such as stiffness, fracture toughness and tensile strength owing to their complex architecture and involvement of organic matter (Currey, 1977, 1999; Jackson et al., 1988; Weiner

and Addadi, 1997). This fact is straightforward because the major function of mollusk shells is protecting their soft bodies (Currey, 1977; Jackson et al., 1988; Kamat et al., 2000). The mechanisms for increasing the mechanical strength of inorganic calcium carbonates can contribute to biomimetics such as technological and biomedical applications (Kaplan, 1998). Another example is that fossil mollusk shells are valuable in stratigraphic and paleoecological studies (Carter, 1990). In addition, the evolutionary histories of mollusks can be estimated from structural and microstructural features of the shells (Taylor and Reid, 1990; Hickman, 2004; Esteban-Delgado, 2008).

1.3 Organic molecules in biominerals

As mentioned above, biominerals contain a certain amount of organic matter and construct organic–inorganic composite structures. Mollusk shells, for example, contain organic components of up to 5% of entire weight, and it is proposed that the mineralization is strongly controlled by the organic matter (Marxen et al., 1998; Marin and Luquet, 2004; Dauphin, 2006). The crystalline phase of the shells is intimately associated with the organic phase, which plays essential roles in crystal formation such as nucleation and growth. Therefore understanding the interactions between crystalline and organic phases is crucially important to illustrate the mineralization processes. Biominerals have been investigated so far using not only crystallographic techniques for the mineral phase but also molecular biological ones for the organic phase. Using the molecular biological techniques, various proteins have been isolated to date. In the case of a pearl oyster, *Pinctada fucata*, a highly acidic protein, Aspein, was identified from

its mantle tissue and suggested to be responsible for calcite deposition, or polymorph selection (Tsukamoto et al., 2004). Another protein, Prismalin-14, was extracted from an acid-insoluble fraction of the prismatic layer in the shells and suggested to play an important role in the regulation of calcification (Suzuki et al., 2004). In addition, a protein named Pif, which specially binds to aragonite crystals and regulates nacre formation, was also identified (Suzuki et al., 2009).

Organic molecules (abbreviated as OMs in this study) in biominerals are conventionally divided into two types, soluble and insoluble fractions during decalcification treatment by acid such as ethylenediaminetetraacetic acid (EDTA). The insoluble OMs basically act as frameworks on which crystals nucleate and grow. We are able to not only observe three-dimensional shapes but also analyze biochemical characteristics of the insoluble OMs by dissolving crystals with acid (Tong et al., 2002; Dauphin et al., 2003a, 2003b). On the other hand, the soluble OMs have been found on the surfaces of the insoluble OMs and inside crystals (Tong et al., 2002). This division is convenient but not appropriate because both fractions share some common features such as amino acid sequences. Hence, I assort OMs into *inter*crystalline and *intra*crystalline OMs in this study, from a mineralogical or crystallographic aspect. Although the intercrystalline OMs are nearly equivalent to the insoluble fraction, they also refer to all OMs that separate crystals. In other words, crystals in both sides of intercrystalline OMs are completely incoherent. The intracrystalline OMs are known as occluded biological macromolecules and often located along specific crystal planes as shown by use of high resolution X-ray diffraction analysis (Berman et al., 1993a, 1993b; Aizenberg et al., 1995a, 1995b). In the case of intracrystalline OMs, crystals in both sides of the OMs are coherent or semi-coherent. Intracrystalline OMs can contain both soluble and insoluble

fractions in the conventional division. Figure 1–11 shows the intercrystalline and intracrystalline OMs in the nacreous layer of *Pinctada fucata* (Suzuki et al., 2011). The intercrystalline OMs exist between aragonite plates and separate the crystals, whereas the intracrystalline OMs are observed inside the aragonite plates.

1.3.1 Intercrystalline organic molecules

The distribution, shapes and chemical compositions of intercrystalline OMs have been actively studied because they can be observed and analyzed by various techniques. In general, scanning electron microscopy (SEM) is suitable to observe and characterize the structural details of intercrystalline OMs. Meanwhile, Weiner and Traub (1980) described the structural characters of the OMs in mollusk shells using X-ray diffraction (XRD). Interlamellar OMs in nacreous structures were identified as chitin by chemical reaction and nuclear magnetic resonance (NMR; Weiss et al., 2002). The OMs in larval

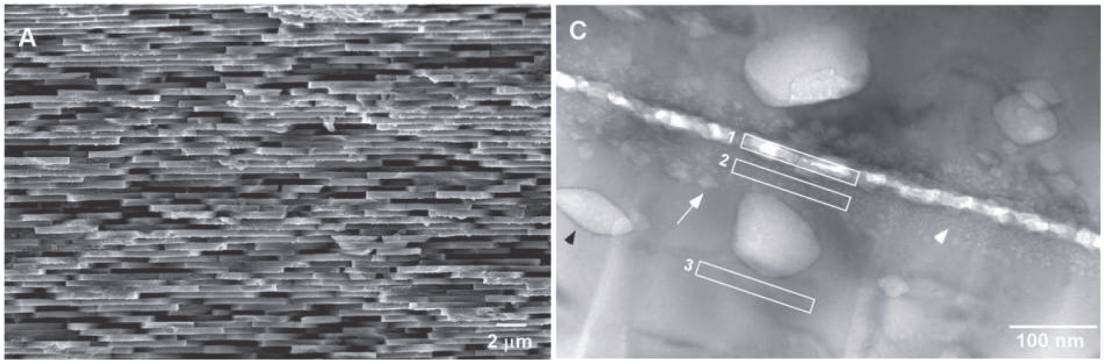

Figure 1–11. (A) SEM images of the fractured nacreous layer of *Pinctada fucata*. (C) Bright-field TEM image (under-focus) of the cross section of the nacreous layer. The white rectangular marked with "1" indicates the intercrystalline OMs that exist between the aragonite plates in (A). The white arrow and arrowhead indicate one of the intracrystalline OMs. (Suzuki et al., 2011).

shells were detected using confocal laser scanning microscopy (Weiss and Schönitzer, 2006). The locations of OMs in nacreous structures were observed by means of immunoelectron microscopy (Nudelman et al., 2006). Fourier transform infrared spectroscopy (FT–IR) can also detect the OMs from the differences of absorption peaks (Hasse et al., 2000).

Intercrystalline OMs are quantitatively the major components of organic matter in mollusk shells. They provide environments in which crystals nucleate, grow and interact with other OMs such as proteins (Weiner and Dove, 2003). Generally three-dimensional frameworks are constructed before crystal deposition by OMs, which become intercrystalline afterward. The frameworks regulate the shapes of crystals and create various kinds of shell structures. In prismatic structures, for example, honeycomb-like OMs are pre-formed, and subsequently crystals fill the holes of the organic frameworks. Consequently, crystals grow like columns that are separated by organic compartment walls, or intercrystalline OMs (Figure 1–12a; Checa et al., 2005). Another example is nacreous structures, in which lamellar organic sheets are pre-formed. Therefore the shapes of crystals intercalated between the sheets are regulated as plates, and finally the architecture like “brick-and-mortar walls” of bivalves and cephalopods, and “stack-of-coins” of gastropods are constructed (Figure 1–12b; Bevelander and Nakahara, 1969; Wise, 1970; Addadi et al., 2006).

In addition, intercrystalline OMs have the function of enhancing the mechanical properties of biominerals. The nacreous structures possess a viscoelastic character and much greater fracture toughness than inorganic crystals. Furthermore, cracks are inhibited in nacre because interlamellar OMs are well bonded to crystals and stretched across the cracks without breaking (Currey, 1977; Jackson et al., 1988).

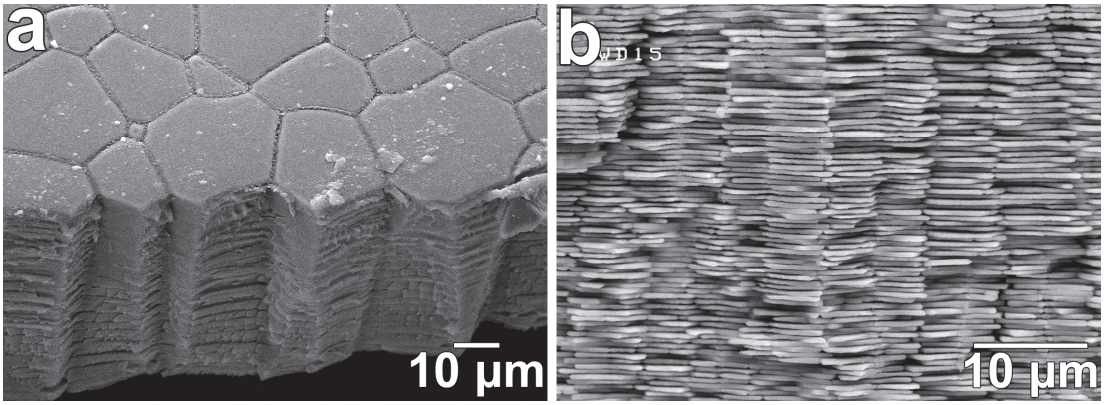

Figure 1–12. SEM images of the prismatic layer of *Pinctada fucata* (a) and the nacreous layer of *Haliotis discus hannai* (b).

1.3.2 Intracrystalline organic molecules

Intracrystalline OMs are also expected to have various influences on the crystal characters of biominerals. Intracrystalline OMs extracted from calcite and aragonite shells of mollusks induce calcite and aragonite *in vitro*, respectively, indicating that they can regulate polymorph selection (Belcher et al., 1996; Falini et al., 1996). Crystal morphology is also modified by intracrystalline OMs extracted from some mollusks and echinoderms because the OMs interact with specific crystal planes (Albeck et al., 1993; Aizenberg et al., 1994). Furthermore, XRD analysis indicated that the calcite crystals of some mollusk shells hold anisotropic lattice distortion and crystallite size, which are ascribed to intracrystalline OMs (Pokroy et al., 2006a).

Intracrystalline OMs also affect the mechanical properties of biominerals. For instance, calcite is the most thermodynamically stable polymorph under ambient conditions, but it easily cleaves along its {104} planes. However, the cleavage planes do not develop on fracture surfaces of biogenic calcite, which exhibits conchoidal fracture

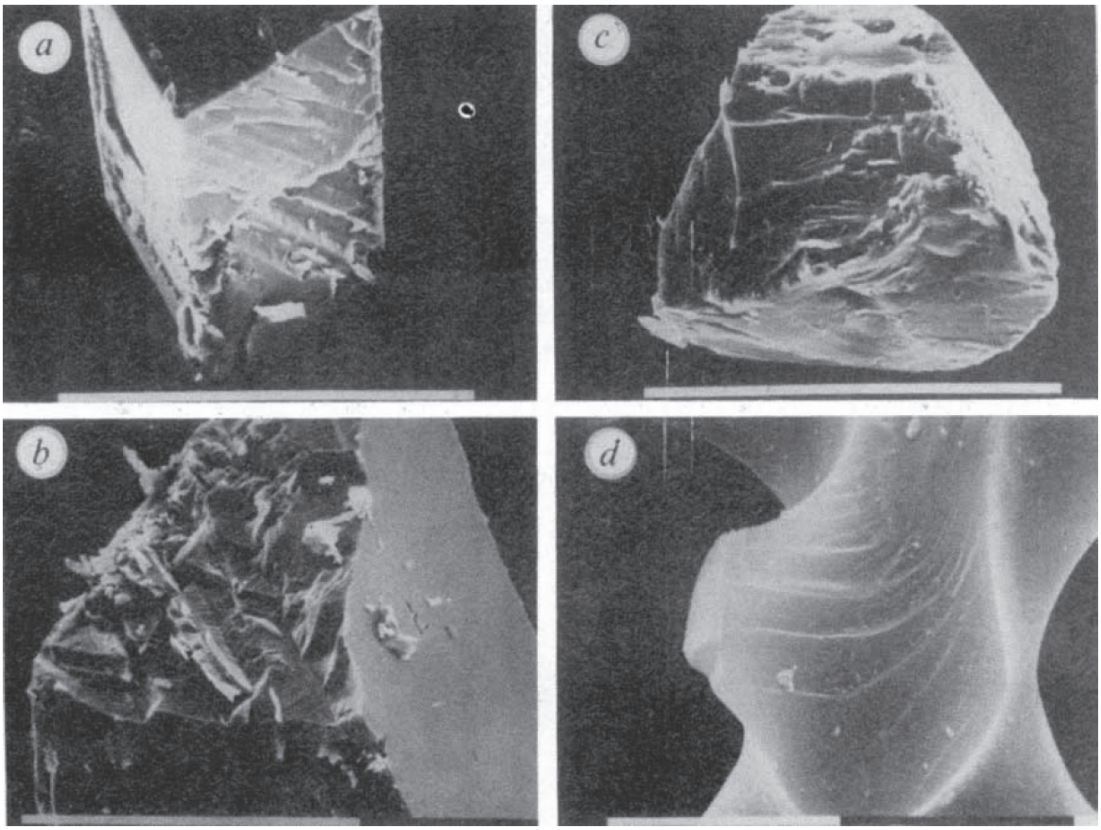

Figure 1–13. SEM images of fractured calcite crystals. (a) Crystals synthesized in the absent of organic molecules, showing {104} cleavage planes. (b) Crystals synthesized in the presence of organic molecules extracted from mollusk shells, showing undeveloped cleavages. (c) Crystals synthesized in the presence of organic molecules extracted from echinoderms, showing glass-like fracture. (d) Sea urchin spine, showing conchoidal fracture. Scale bar: 10 μm. (Berman et al., 1988).

instead (Figure 1–13; Berman et al., 1988). This phenomenon was reproduced in the crystals synthesized in the presence of OMs *in vitro* (Kim et al., 2011). Furthermore biogenic calcite is known to be harder and tougher than abiogenic one. Such improvement of mechanical properties in biogenic calcite is attributed to OMs inside crystals (Emlet, 1982; Aizenberg et al., 1997; Robach et al., 2005; Kunitake et al., 2013).

Thus there are many studies that reported the influence of intracrystalline OMs on crystal structures and characters, but information where the OMs are located or distributed inside crystals is limited because it is difficult to observe them by using SEM and other microscopic techniques. Furthermore, the interactions and relationships between crystals and intracrystalline OMs have been scarcely examined because of unestablished analytical methods.

1.4 Visualization of intracrystalline organic molecules

Although it is difficult to detect intracrystalline OMs using microscopic analytical methods, recent high-resolution techniques enable us to observe them directly. Gordon and Joester (2011) applied pulsed-laser atom-probe tomography to the tooth of a mollusk, the chiton *Chaetopleura apiculata*, and revealed three-dimensional chemical maps of OMs inside magnetite crystals. Carbon was recognized as a constituent of OMs inside the surrounding iron and oxygen in the mineral phase. Analyzable volumes are rather small (up to approximately 10^5 nm^3), but atom probe tomography is a powerful tool for obtaining information on the chemical composition with subnanometer spatial resolution (Kelly and Miller, 2007). However, the mineral phase of the mollusk shells investigated in this study is composed of calcium carbonate crystals, therefore we are unable to distinguish carbon of the mineral phase from that of the organic one using this method.

Instead, electron beam techniques have been used to visualize OMs inside calcium carbonate biominerals. Void-like contrasts in biomineral crystals were observed

using transmission electron microscopy (TEM) in the past, but they were interpreted as heat-induced artifacts caused by electron beams or ion beams during sample preparation (Towe and Thompson, 1972; Velázquez-Castillo et al., 2006). However, energy-dispersive X-ray spectroscopy (EDS) and electron energy-loss spectroscopy (EELS) have recently revealed that these contrasts correspond to OMs (Gries et al., 2009; Okumura et al., 2010; Suzuki et al., 2011). Now intracrystalline OMs can be visualized by two kinds of electron microscopy imaging; TEM imaging and high-angle annular dark-field (HAADF) imaging with scanning TEM (STEM). Electron microscopic analyses adopted in this study for visualizing intracrystalline OMs are described below.

1.4.1 Fresnel contrasts in TEM

In TEM images, intracrystalline OMs are observed as Fresnel contrasts (Figure 1–14; Robach et al., 2005; Gries et al., 2009; Okumura et al., 2010; Suzuki et al., 2011; Younis et al., 2012). The Fresnel contrasts basically arise in the same manner as "Fresnel fringes," which are observed at the edges of specimens or holey carbon membranes on microgrids. The Fresnel fringes are produced when spherical waves scattered from the edges interfere with incident waves (Figure 1–15; Horiuchi, 1988). Fresnel contrasts appear only when the objective lens is not focused on the bottom surface of a specimen, namely out of focus. The intensity of the contrasts depends on the differences of the electrostatic potential between inclusion and surrounding materials. When images are under-focused ($\Delta f < 0$), the Fresnel contrasts at small inclusions become bright dots surrounded by dark fringes, on the contrary, when over-focused ($\Delta f > 0$) they become

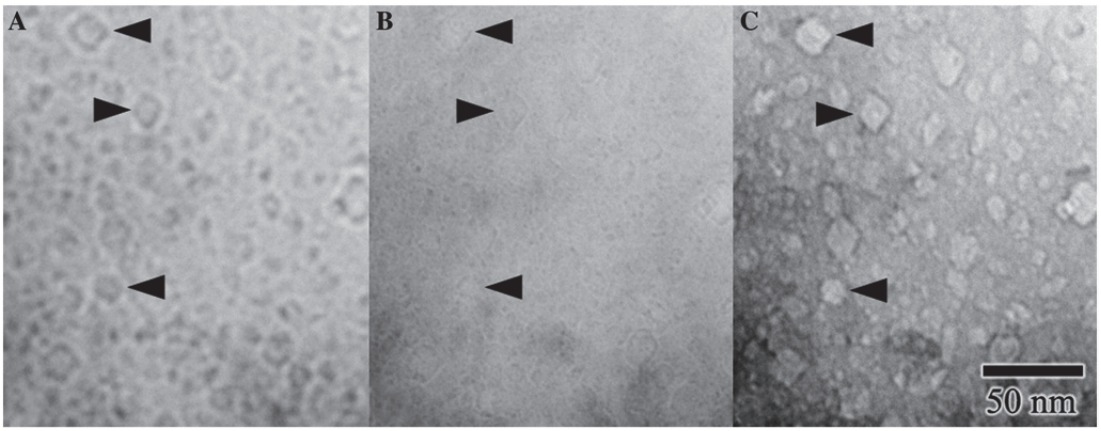

Figure 1–14. TEM images showing the Fresnel contrasts of OMs in the tooth of a sea urchin, *Lytechinus variegatus*. (A) Over-focused image. (B) In-focus image. (C) Under-focused image. Arrowheads indicate the same OMs in all three images. (Robach et al., 2005).

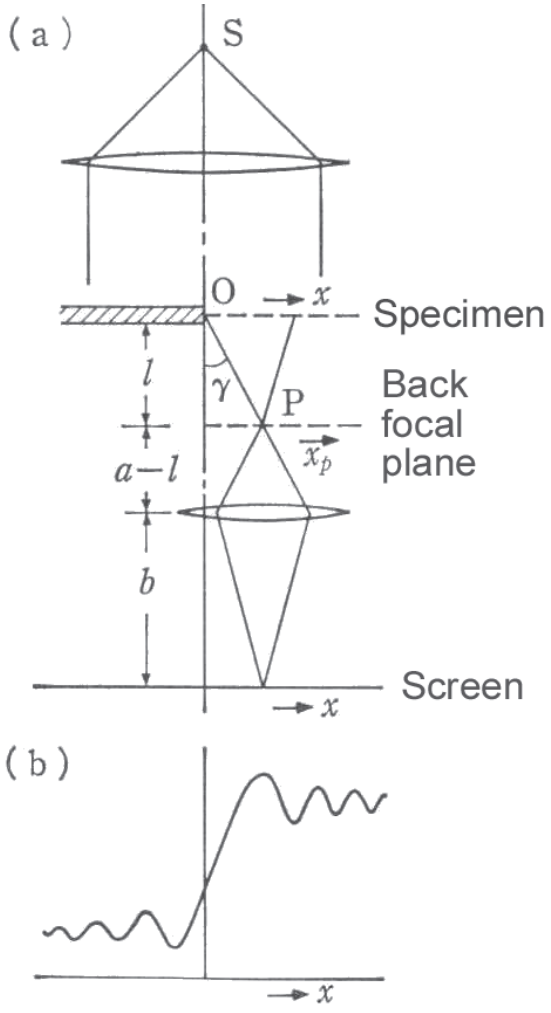

Figure 1–15. Electron beam path (a) and contrast intensity (b) in an over-focused condition. (Adapted from Horiuchi, 1988).

dark dots with bright fringes (Williams and Carter, 2009).

1.4.2 Z-contrast in HAADF–STEM

STEM imaging techniques were developed by combining TEM and SEM technologies. A series of lenses focuses an electron beam to form a small spot, or probe, incident upon electron-transparent specimens. Scan coils are arranged to scan the probe over the specimens, and various scattered electrons are detected and their intensity is plotted as a function of probe positions to form a magnified image. In a bright-field mode, transmitted electrons that leave the specimens at the same or lower angles with respect to the optic axis are collected. In an annular dark-field mode, on the other hand, scattered electrons that leave the specimens at higher angles with respect to the optic axis are collected using an annular detector (Figure 1–16). In HAADF–STEM imaging, the annular detector collects electrons scattered over an angular range more than several tens of milliradians. In the region of high scattering angles (ca. 100 mrad), the scattered electrons are no longer coherent because most of them are originated from thermal diffuse scattering due to thermal vibrations of the specimen atoms. Consequently, contrast in HAADF–STEM images is roughly dependent on the square of the atomic number (Z), or Z-contrast (Pennycook and Nellist, 2011). This imaging technique has been applied to biominerals recently. OMs inside biominerals are observed as dark contrasts because OMs are lower-Z materials than surrounding crystals such as calcium carbonate (Figure 1–17; Gries et al., 2009; Li et al., 2011; Younis et al., 2012).

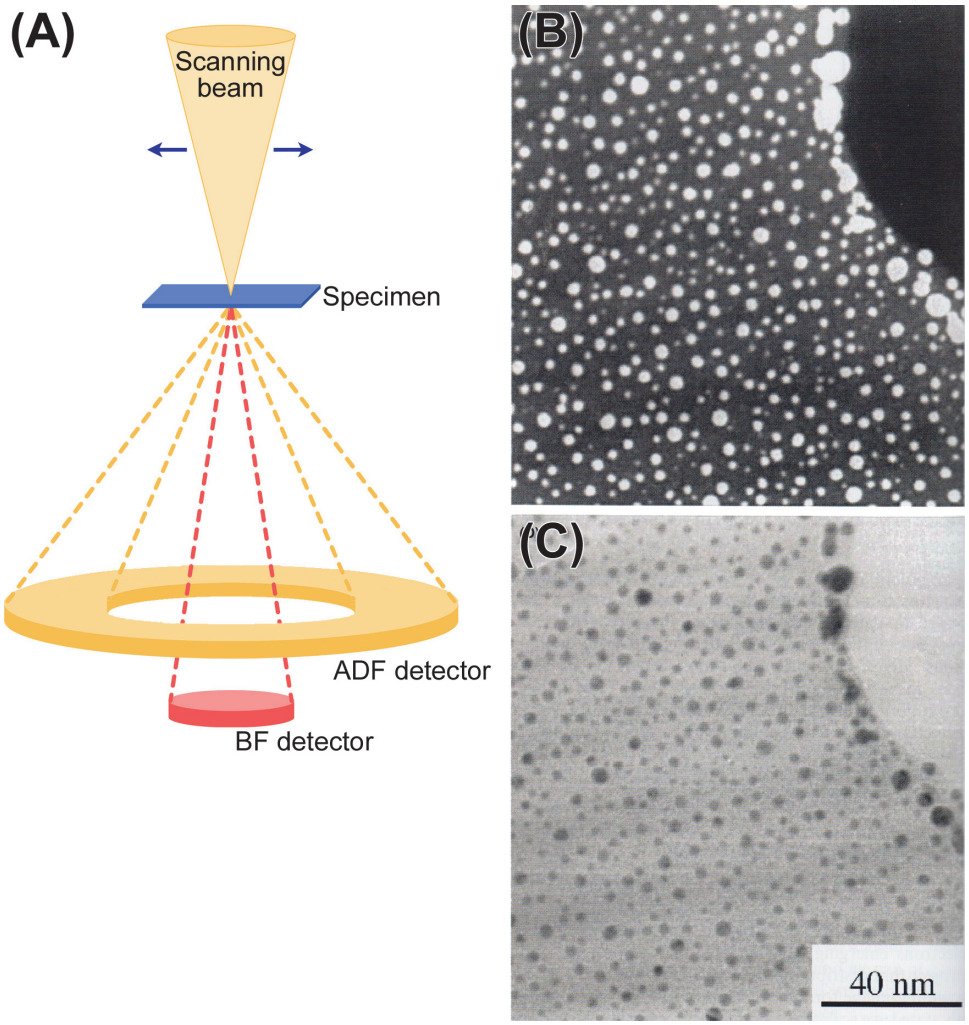

Figure 1–16. (A) Schematic showing STEM image formation. ADF: annular dark-field. BF: bright-field. Au particles on a carbon film in the ADF image (B) and the BF image (C). (B, C: adapted from Williams and Carter, 2009).

Figure 1–17. HAADF–STEM image of the nacreous structure in a mollusk shell, *Perna canaliculus*, showing interlamellar and intracrystalline OMs as dark contrasts. (Younis et al., 2012).

1.4.3 EELS

Energy distribution of electrons that have gone through a specimen is analyzed by EELS. These electrons may have lost no energy or suffered inelastic collisions. These energy-loss events tell us various information about the chemistry and electronic structure of the specimen atoms, e.g., their bonding/valence states, nearest-neighbor atomic structure, free-electron density, and specimen thickness. A magnetic-prism spectrometer is used to obtain the electron energy spectra (Figure 1–18). The electrons that have passed through the specimen travel down a drift tube and are deflected by ≥ 90° by a magnetic field. The electrons that have lost energy are deflected further than those with no energy loss. The electrons suffering the same energy loss are brought back to the same position on a dispersion plane of the spectrometer even though they have traveled in on-axis or off-axis directions. Thus spectrum of distribution of electron

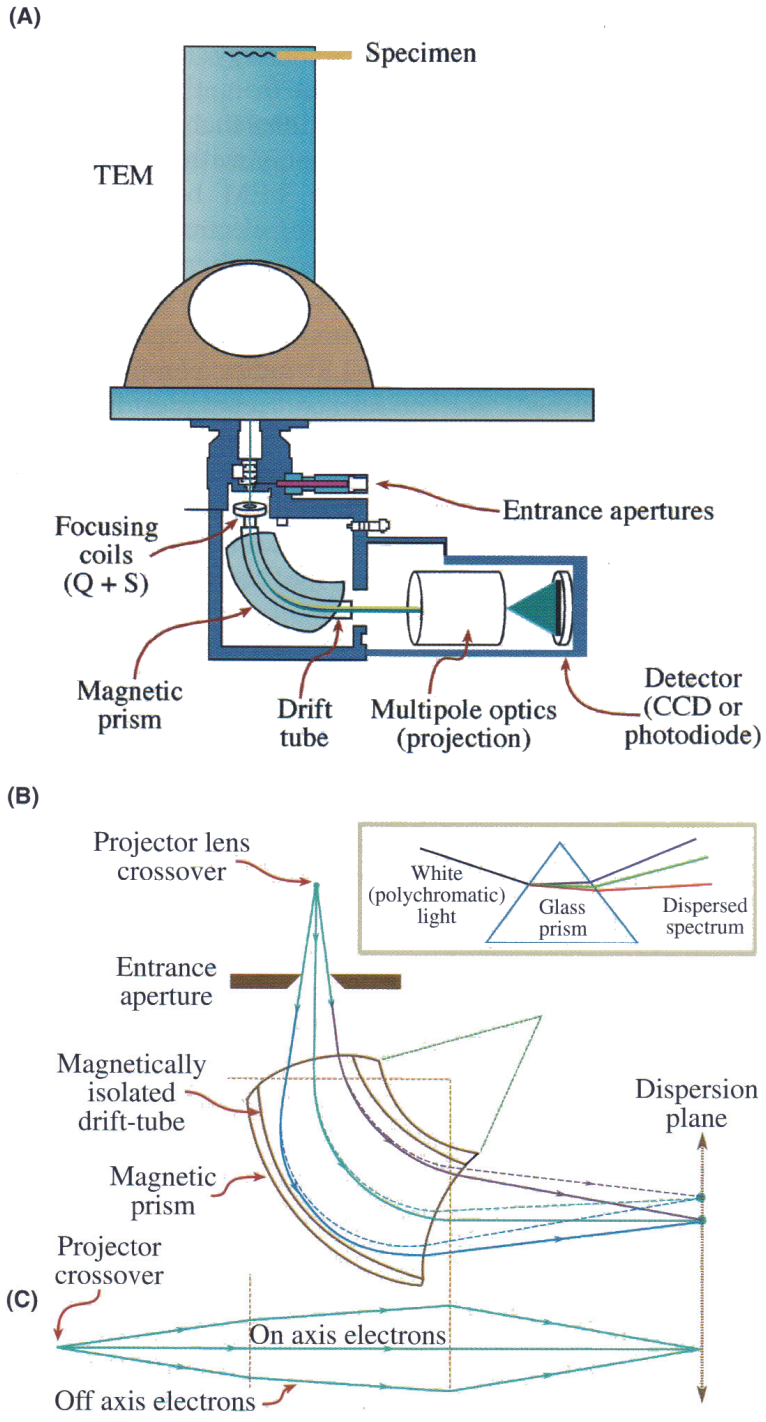

Figure 1–18. (A) Schematic showing an EELS below a viewing screen of a TEM. (B) Ray paths through a magnetic prism spectrometer showing the different dispersion and focusing of the zero-less and energy-loss electrons on the dispersion plane of the spectrometer. Inset shows the analogy with the dispersion of white light by a glass prism. (C) The lens focusing action in the plane normal to the spectrometer. (Williams and Carter, 2009).

intensity versus energy loss is formed on the dispersion plane. When EELS analysis is applied to biominerals that are composed of calcium carbonate, carbon in organic phases can be distinguished from that for carbonate ions (CO_3^{2-}) by analyzing the near edge structure of the carbon K-edge, which is interpreted in terms of electronic transitions from the 1s state to the antibonding molecular orbital states (Figure 1–19; Martin et al., 1989, 1996; Varlot et al., 1997, 1999; Mansot et al., 2003). In the case of carbonate materials, the carbon K-edge presents a sharp peak at 289 eV and a broad peak at 299 eV corresponding to the electron transitions from 1s to π^* (C=O) and σ^* (C–O) bonds, respectively. For amorphous carbon, graphite and organic matter, on the other hand, an intense peak appears at 284 eV, which is attribute to the electron transition from 1s to π^* (C=C) bonds. Thus the peak at 284 eV is regarded as the fingerprint of organic phases in calcium carbonate biominerals. The EELS instrument equipped in a STEM enables us to obtain spectra from nanometer-sized OMs inside the crystals.

1.4.4 HAADF–STEM tomography

Electron tomography has matured into a technique that is used widely to investigate the three-dimensional (3D) structure of many kinds of materials. In general, tomographic reconstruction using backprojection relies on the premise that the intensity in projections is a monotonic function of the physical quantity to be reconstructed. This is known as the “projection requirement.” To meet the projection requirement, crystalline materials should be studied using a tomography technique that minimizes diffraction contrast. Images with minimal Bragg diffraction contrast can be formed in a STEM

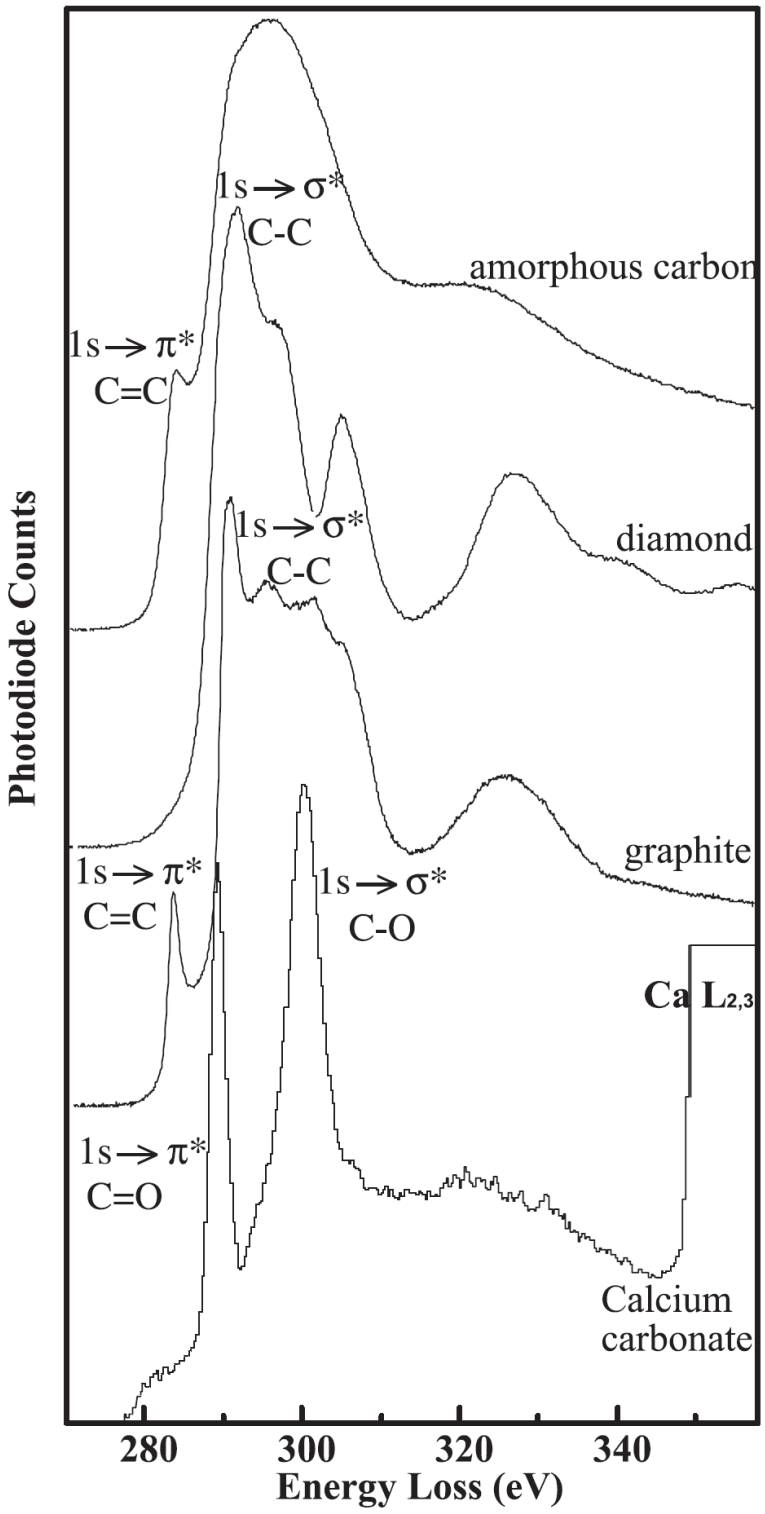

Figure 1–19. EELS spectra of various carbon species. Carbon K-edge in amorphous carbon, diamond, graphitic carbon and calcium carbonate. (Mansot et al., 2003).

mode by increasing the inner radius of an annular dark-field detector so as to exclude coherent electrons, namely HAADF imaging. The lack of coherence in HAADF images means that the images can be considered as projections of the structure in terms of thickness and atomic number, and thus they meet the projection requirement for tomographic reconstruction. The tomography with HAADF–STEM imaging recently revealed the 3D shapes and distribution of intracrystalline OMs in mollusk shells (Younis et al., 2012). For instance, Li et al. (2011) showed that OMs in calcite crystals of a mollusk shell, *Atrina rigida*, are aligned roughly perpendicular to the crystallographic *c*-axes, and discussed the interactions between crystals and OMs.

1.5 Purpose of this study

As stated above, the interaction between crystals and OMs is the most fundamental problem in biomineralization. The issues that arose from previous studies on the organic–inorganic interactions are integrated into the following two points:

- Although intracrystalline OMs as well as intercrystalline ones have great influence on the host inorganic crystals, their distribution and locations are not well characterized. Hence we do not have enough information how OMs are incorporated into crystals.
- Although recent high-resolution techniques enable us to visualize intracrystalline OMs at a nanoscale, the roles of the OMs which induce particular microstructures and properties of biominerals have scarcely been

understood at the same scale.

I mainly investigated the crystallographic features of the calcite crystals constituting the prismatic layer in a pearl oyster, *Pinctada fucata*, in my master's course (Okumura et al., 2010). In the prismatic layer, columnar crystals are individually separated by organic compartment walls, or intercrystalline OMs (Grégoire, 1961; Wada, 1961; Kennedy et al., 1969), and arranged with their crystallographic *c*-axes perpendicular to the shell surfaces (Figure 1–20; Taylor et al., 1969; Checa et al., 2005; MacDonald et al., 2010). SEM observation of "honeycomb" structure on the internal surfaces of the shells revealed that each prism is divided into several domains by sinuous grooves (Figure 1–21). Misorientation angles between both sides of grooves are approximately 10° according to electron back-scattered diffraction (EBSD) analysis, indicating that columnar prisms exhibit a polycrystalline feature (Figure 1–22). Furthermore the crystals within the domains are not monolithic single crystals but have gradual orientation change by several degrees. The structure of steep and gradual orientation change inside prisms was recently reported using EBSD mapping also in *Pinctada margaritifera*, which is a species related to *Pinctada fucata* (Checa et al.,

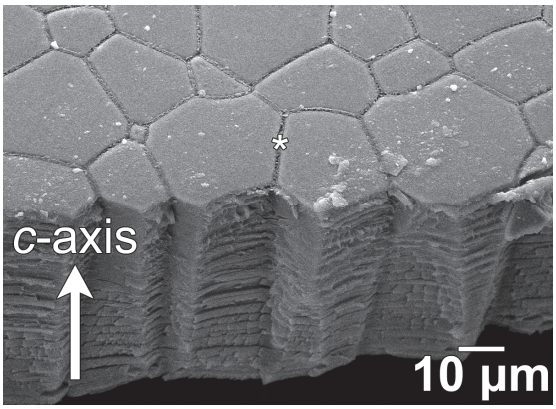

Figure 1–20. SEM image of the prismatic structure in a pearl oyster, *Pinctada fucata*. * indicates the locations of intercrystalline organic walls.

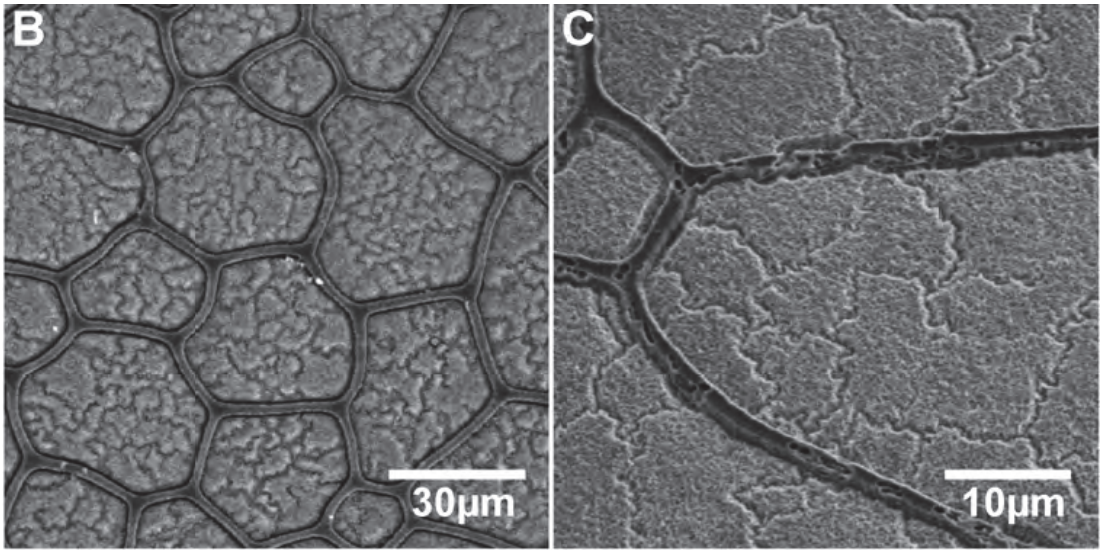

Figure 1–21. SEM images of the internal surfaces of prismatic structure in a pearl oyster, *Pinctada fucata*, showing sinuous grooves divide the prisms into domains (B). (C) Enlarged image of the grooves. (Okumura et al., 2010).

2013). Such materials are very intriguing because the gradual orientation change can improve the mechanical properties of crystals (Olson et al., 2013). On the other hand, in the case of the prisms in another bivalve shell, each prism shows a single-crystalline feature (Dauphin, 2003; Dauphin et al., 2003a). The origin of the difference is probably related to intracrystalline OMs.

Considering the issues raised above and their linkage with my previous research, I focused on the calcite crystals constituting outer layers of mollusk shells and set the following goals for my study:

1. To show the distribution and locations of intracrystalline OMs at a nanoscale.
2. To reveal the influence of intracrystalline OMs on microstructure of crystals.
3. To deliberate upon the interactions between crystals and intracrystalline OMs.

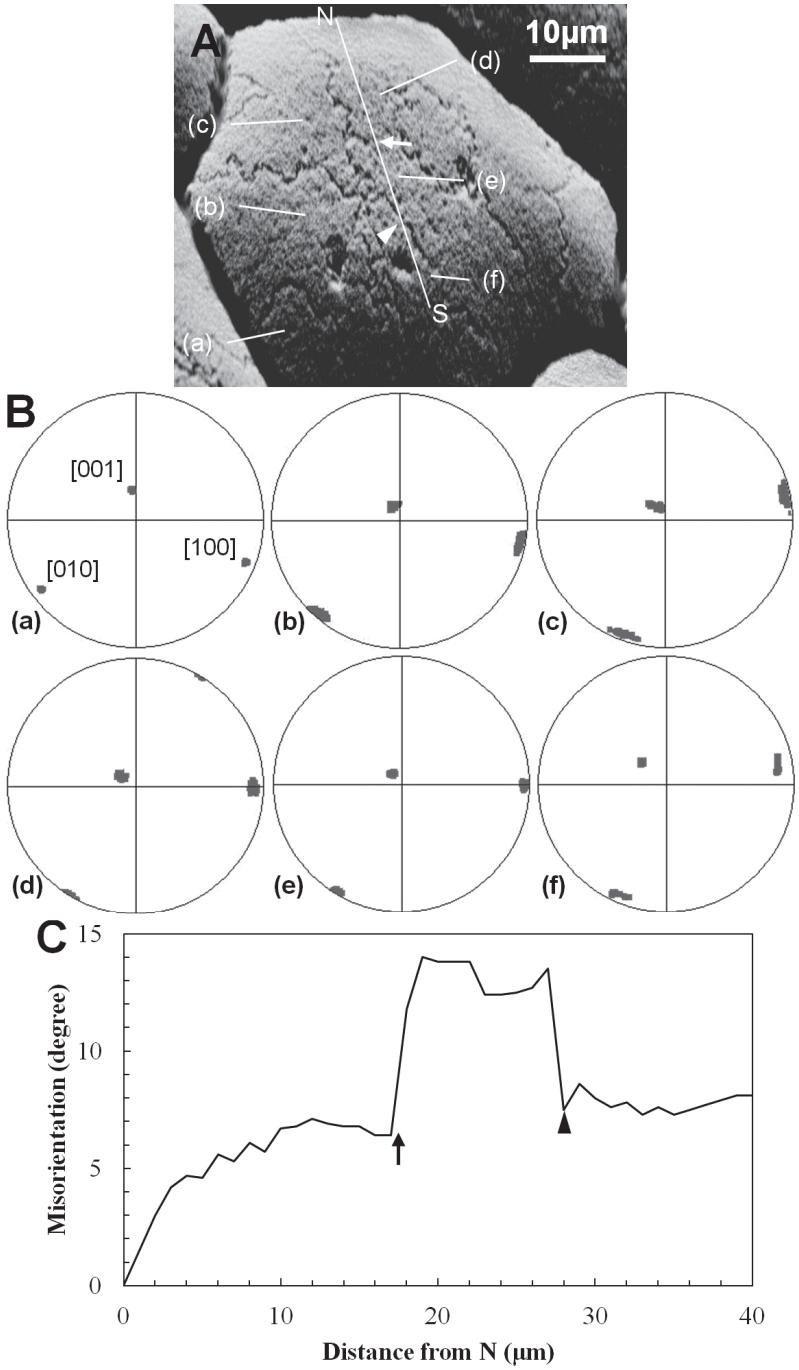

Figure 1–22. (A) SEM image of the prism in *Pinctada fucata* analyzed by EBSD. Six domains divided by the sinuous grooves are denoted by (a)–(f). (B) Pole figures (upper hemisphere) for each domain of (a)–(f) indicated in (A). The directions of [001], [100] and [010] of calcite are plotted. (C) Misorientation profile along the line NS in (A). Arrow and Arrowhead indicate the positions of the grooves indicated in (A). Crystal orientation change steeply at the grooves by approximately 10° and gradually within the domains by several degrees. (Okumura et al., 2010).

To achieve these goals, two approaches were adopted in this study. One is examining the relationships between crystals and intracrystalline OMs from detailed observation of mollusk shells. This investigation is described in Chapter 2. The other is synthetic experiments in which calcium carbonate crystals were formed *in vitro* in the presence of OMs extracted from mollusk shells. The influence of the extracted OMs on crystal structure is explicated in Chapter 3. Finally I organize the results obtained from the two approaches and propose a mechanism whereby inter- and intracrystalline OMs regulate crystal structure in biomineralization processes in Chapter 4.

Chapter 2.

Microstructural control with intracrystalline organic molecules in mollusk shells

2.1 Chapter introduction

2.1.1 Microstructures of mollusk shells

The diverse microstructures of mollusk shells are now categorized by many researchers (e.g., Taylor et al., 1969; Carter, 1990b). The classification of them into seven microstructural groups (prismatic; spherulitic; laminar; crossed; homogeneous; isolated spicules and spikes; and isolated crystal morphotypes) and six microstructural categories (aragonitic prismatic; calcitic prismatic; nacreous aragonitic; porcelaneous aragonitic; foliated; and calcitic) were proposed by Carter (1980). Afterward, the terms and definitions concerning the shell microstructures were described in detail in a glossary (Carter, 1990a). Although this glossary is certainly rigorous, it contains too many classes for other scientific fields than taxonomy to discuss them. In contrast, Grégoire (1972) introduced concise classification based on SEM and TEM observations: homogeneous; prismatic; foliated; nacreous; grained; crossed-lamellar; and complex crossed-lamellar. Recently de Paula and Silveira (2009) reformed and simplified this concept, and created the classification of five principal microstructures: prismatic; crossed-lamellar; nacreous; homogeneous; and spherulitic.

2.1.2 Shell structures of mollusks investigated in this study

The outer layers of mollusk shells are generally either aragonite or calcite prismatic structure (Lutts et al., 1960). In this study, I have concentrated to examine the calcite prismatic structures of six shells: a pearl oyster (*Pinctada fucata*); a winged oyster

(*Pteria penguin*); a pen shell (*Atrina pectinata*); and an oyster (*Crassostrea nippona*) as bivalve shells; an abalone (*Haliotis discus hannai*) and a limpet (*Collisella dorsuosa*) as gastropod shells. The prismatic structure is further divided into four categories by Carter (1980): simple prismatic; fibrous prismatic; spherulitic prismatic; and composite prismatic. The calcite prismatic structures of the above four bivalve shells belong to the simple prismatic structure. *Pinctada*, *Pteria* and *Atrina* shells are composed of two layers: outer simple prismatic structure in which columnar crystals are perpendicular to the shell surfaces as shown in Figure 1–20; and inner aragonite nacreous structure. Although *Crassostrea* shells also consist of principal two layers, outer prisms are inclined at approximately 30° especially in the outer part of the shells, and the inner layer is calcite foliated structure containing calcite chalky lenses and myostracal aragonite prisms (Figure 2–1; Tsujii et al., 1958; Watabe and Wilbur, 1961; Checa et al.,

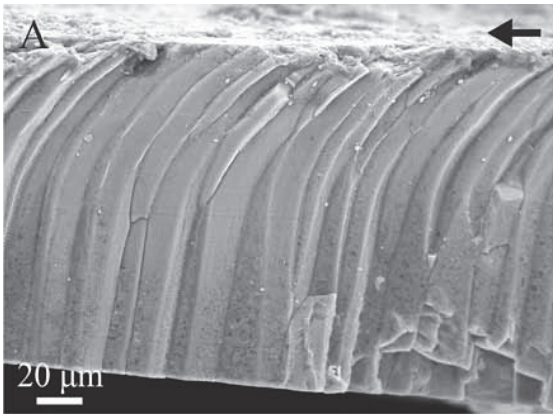

Figure 2–1. SEM image of the cross section of inclines simple prismatic structure in *Ostrea edulis*, which is related to *Crassostrea nippona*. (Checa et al., 2009).

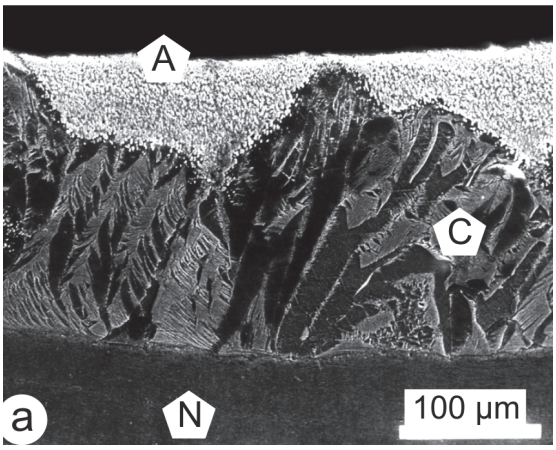

Figure 2–2. SEM image of the cross section of *Haliotis tuberculata*, which is related to *Haliotis discus hannai*. A, C and N indicate aragonite prismatic, calcite prismatic and aragonite nacreous layers, respectively. (Dauphin et al., 2005).

2009). In the case of the gastropod shells, the outer layers of *Haliotis* and *Collisella* are composite and spherulitic prismatic structures, respectively. *Haliotis* shell also has an inner aragonite nacreous layer. In addition, aragonite prismatic structure exists at the outmost part of the shells as a superficial layer (Figure 2–2; Hedegaard, 1997; Dauphin et al., 2005). The structure of *Collisella* is composed of extremely complicated, five-layered structure, but calcite crystals exist only at the outmost spherulitic prismatic layer named M + 3 (Figure 2–3; Fuchigami and Sasaki, 2005; Suzuki et al., 2010). It should be noted that calcite crystals constituting the prismatic structures are formed as the outer layers in all shells, indicating that the prisms are initially formed parts in the shell formation processes. Since the prismatic structures are formed first as the outer layers when the shells are still immature, they are structurally important to protect their soft bodies efficiently.

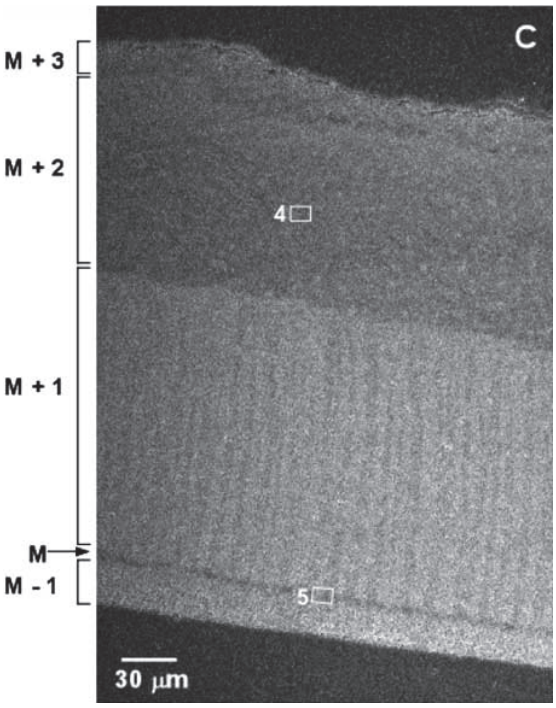

Figure 2–3. SEM image of the cross section of *Lottia kogamogai*, which has the same layered-structure as *Collisella dorsuosa*. It has five layers: M + 3; M + 2; M + 1; M; M − 1. Only M + 3 layer is calcite. (Suzuki et al., 2010).

2.1.3 Contents of this chapter

This chapter is composed of two parts. The crystallographic characteristics of biogenic calcite in the mollusk shells are described in the first part (Chapter 2A). The second part (Chapter 2B) focused on the three-dimensional distribution of intracrystalline OMs in the shells. Finally these two parts are summarized and discussed together.

2A. Crystallographic study on calcite crystals constituting outer layers of mollusk shells

2A.1 Introduction

This chapter focuses primarily on the calcite prismatic structure of *Pinctada*. *Pinctada* has received a great deal of attention especially from Japanese researchers because of its importance in pearl industries. As a result, the structure of the shell and the processes of calcification for this species are known better than those for other mollusks. First I investigated the crystallographic microstructures of the calcite prisms of *Pinctada* in detail, as well as those of *Atrina* for comparison. Subsequently other prisms in *Pteria*, *Crassostrea*, *Haliotis* and *Collisella* were also examined.

As stated above, each prism of *Pinctada* and *Atrina* is separated by a thick organic compartment wall and arranged with its crystallographic *c*-axis perpendicular to the shell surfaces, or periostracum. The prisms show a so-called "honeycomb" pattern in a planar view, and indicate geometrical selection in a cross-sectional view in *Pinctada*, in other words, prisms with slower growth rates along the direction perpendicular to the shell surface wedge out and they become fewer in number and larger in size (Taylor et al., 1969; Carter, 1990a). However, the geometrical selection has never been observed in *Atrina* prisms, which are completely columnar (Checa et al., 2005).

Although each prism of *Pinctada* consists of several domains divided by sinuous grooves as mentioned in Chapter 1, the prisms in *Atrina* show a monolithic

single-crystalline feature (Figure 2–4; Dauphin, 2003; Dauphin et al., 2003a). Furthermore the intraprismatic domains in *Pinctada* have gradual orientation change by several degrees. Figure 2–5 shows the amount of local lattice strain in several biogenic calcite estimated by XRD analysis. The local lattice strain is greater in the prisms of

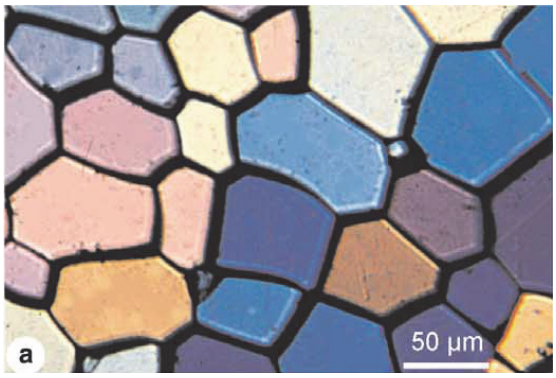

Figure 2–4. Polarized light microscopy image of the inner surface of the prisms in *Pinna nobilis*, which is related to *Atrina pectinata*. The individual prisms are monolithic single crystals. (Dauphin et al., 2003).

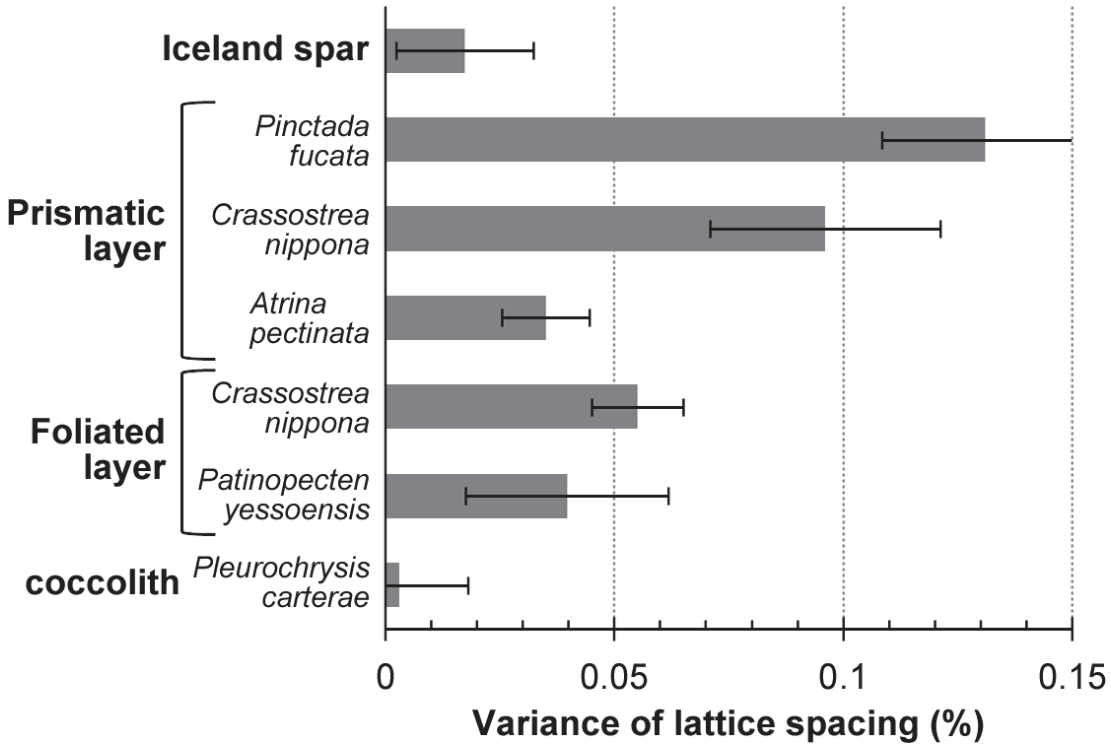

Figure 2–5. Variance of lattice spacing (local lattice strain) determined by XRD analysis with Williamson–Hall plots. (Adapted from Okumura et al., 2012).

Pinctada than *Atrina*, indicating some structural difference between the two shells (Okumura et al., 2012). Such larger lattice strain in *Pinctada* may be attributed to intracrystalline OMs, but the prisms of *Atrina* contain the similar amount of OMs to *Pinctada*, as shown by thermogravimetric analysis (Figure 2–6; Okumura et al., 2012). Therefore, some factors other than the amount of OMs should contribute to the gradual orientation change and the local lattice strain in *Pinctada*. To reveal these factors, I conducted micro- and nanoscopic examination of these shells.

First of all, I conducted nanoindentation tests to characterize the mechanical properties of the prisms of *Pinctada* and *Atrina*. Next TEM/STEM imaging and XRD analysis were carried out to reveal the influence of intracrystalline OMs on crystal

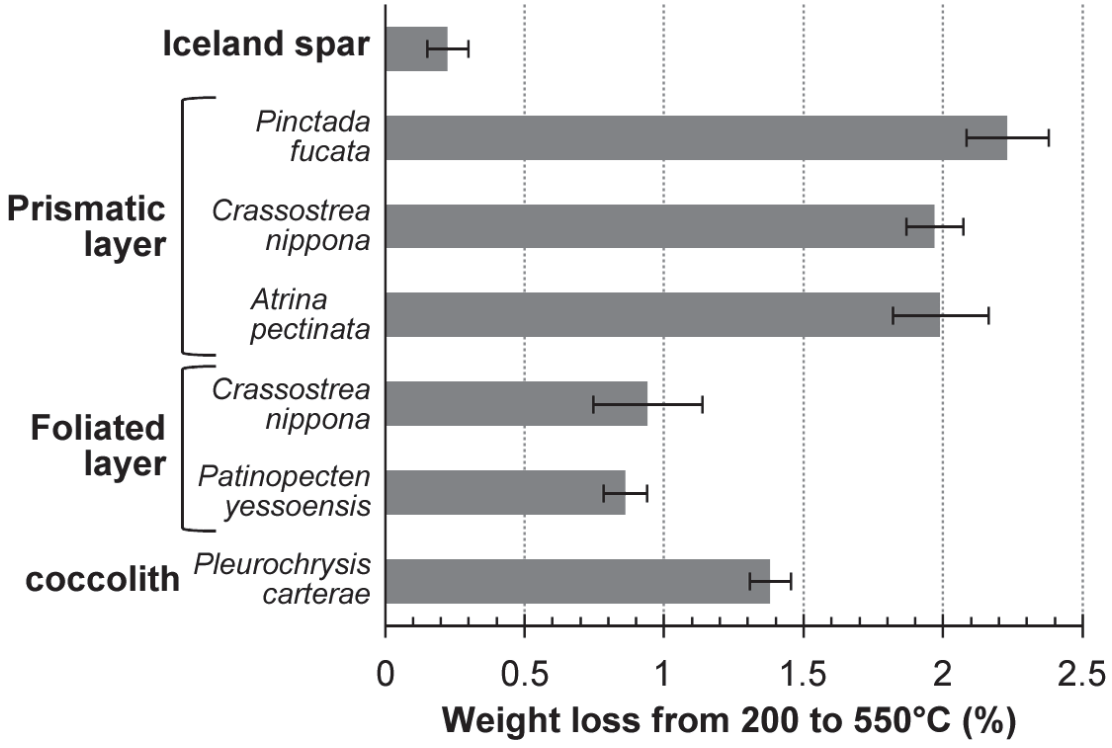

Figure 2–6. Weight loss of various calcite crystals from 200 to 550°C, indicating the amount of intracrystalline OMs. (Adapted from Okumura et al., 2012).

structures. Then the prisms of *Pteria*, *Crassostrea*, *Haliotis* and *Collisella* were compared with the two shells in order to reveal the general strategy of shell formation adopted by mollusks.

2A.2 Materials

In the present study, I investigated the calcite crystals of four bivalve shells (*Pinctada fucata*, *Pteria penguin*, *Atrina pectinata*, and *Crassostrea nippona*) and two gastropod shells (*Haliotis discus hannai* and *Collisella dorsuosa*). The shells of *Pinctada* and *Haliotis* were supplied by Mie Prefecture Fisheries Research Institute, those of *Pteria* by TASAKI & Co., Ltd., and those of *Crassostrea* by Akita Prefectural University. The shells of *Collisella* were collected in Jogashima Island, Kanagawa prefecture, Japan, and those of *Atrina* were obtained at Tsukiji Market, Tokyo, Japan. The shells were dried off after their soft inner parts were removed. In addition, Iceland spar, a transparent geological calcite crystal with perfect rhombohedral morphology, was investigated as a representative of abiogenic calcite.

2A.3 Methods

Nanoindentation

Since intracrystalline OMs are expected to have significant influence on mechanical properties of biogenic calcite (Emlet, 1982; Kim et al., 2011), the difference of micro-mechanical properties between *Pinctada*, *Atrina* and Iceland spar was assessed by a nanoindentation technique. Nanoindentation tests need to be performed on smooth and damage-free surfaces for avoiding variations in results. For this reason, the surfaces of calcite crystals were polished initially with silicon carbide powder (32, 13 and 8 μm), then with diamond suspension (1 μm), and finally with colloidal silica (0.06 μm). In addition, all tests were performed on the crystallographic (001) planes of calcite for avoiding crystal orientation dependence of the results. Since the calcite prisms of the investigated shells are arranged with their *c*-axes perpendicular to the shell surfaces, the inner surfaces of the prisms almost correspond to the (001) planes. In the case of Iceland spar, the crystals were cut to exhibit its (001) planes before polishing. The nanoindentation experiments were performed using a depth-sensing nanoindenter, DUH-211 (Shimadzu). The indenter was a triangular-pyramidal diamond tip with a tip angle of 115°. All tests were programmed in a way that loading started when the indenter came into contact with a test surface and the load maintained 10 sec at the maximum load of 100 mN before unloading. The loading speed was 4.4 mN/sec. After the nanoindentation, the impressions made by the indenter were examined using SEM. SEM observation was carried out using an S-4500 SEM (Hitachi) with a cold field-emission gun at an acceleration voltage of 5 kV. SEM specimens were coated with

Pt–Pd before observation.

TEM observation

The specimens for TEM observation were prepared using an FB-2100 focused ion beam (FIB) system with a micro-sampling system (Hitachi High-Technologies). Fragments of the bivalve shells and cross-sectional specimens of the gastropod shells were prepared. For the cross-sectional specimens, fragments of the shells embedded in epoxy resin were cut with a diamond saw, and subsequently polished to avoid subsurface deformation. They were coated with carbon before loading into an FIB instrument. The specimens were locally coated with tungsten for preventing beam damage during fabrication. They were subsequently trimmed using a gallium ion beam of 30 kV, and thinned down to be electron-transparent with a low energy beam of 10 kV as a final process. TEM observation was conducted using a JEM-2010UHR TEM (JEOL) operated at 200 kV for gaining crystallographic information of the shells at a nanoscale.

STEM–EELS analysis

EELS analysis was conducted using an Enfina spectrometer (Gatan) equipped to a JEOL JEM-2010F TEM (JEOL) with a field-emission gun operated at 200 kV, in order to verify that Fresnel contrasts in the crystals correspond to organic matter. Specimens were prepared using FIB in the same manner as those for TEM observation, and cleaned using a JIC-410 ion cleaner (JEOL) just before the analyses to avoid contaminations. Since each Fresnel contrast was very small, EELS spectra were obtained from

nanoscopic areas (< 10 nm) by converging the electron beam in a STEM mode. Each spectrum was collected within 5 seconds to avoid radiation damage, and approximately 30 spectra were collected and integrated with attention to the energy shift. HAADF–STEM imaging was also conducted simultaneously.

XRD analysis

As complementary and macroscopic characterization of the crystallographic aspect, XRD analysis was also conducted for the prisms of *Pinctada* and *Atrina*. Powder XRD patterns were obtained using a RINT-Ultima$^+$ diffractometer (Rigaku) with Cu Kα radiation emitted at 40 kV and 30 mA. A D/teX Ultra module with a silicon strip detector (Rigaku) was equipped to the instrument, which enabled us to obtain X-ray counts about a hundred times higher than a conventional scintillation counter. Cu Kβ was eliminated by Ni foil. To improve the signal-to-noise ratio, a nonreflecting silicon sample holder was used. A 0.25° divergence slit, a 5 mm mask for confining the beam width, and an 8 mm anti-scatter slit were adopted. A scan rate was 0.1° (2θ)/min and data was collected at every 0.01° (2θ). Local lattice strain ($\Delta d/d$) and coherence length (L) was estimated using Williamson–Hall plots (Hall, 1949; Williamson and Hall, 1953) as follows:

$$\frac{\Delta(2\theta)\cos\theta}{\lambda} = \left(\frac{\Delta d}{d}\right)\frac{2\sin\theta}{\lambda} + \frac{0.94}{L}$$

where θ is the Bragg angle of the analyzed peak, $\Delta(2\theta)$ is the full-width at half-maximum (FWHM) of the peak, and λ is the X-ray wavelength. The contribution of Cu $K\alpha_2$ to FWHM was removed by the Rachinger's method with a program installed in the XRD instrument, assuming that the intensity ratio of $K\alpha_2/K\alpha_1$ is 0.4970. Plotting the

values of $[\Delta(2\theta)\cos\theta/\lambda]$ as a function of $(2\sin\theta/\lambda)$, the local lattice strain ($\Delta d/d$) and coherence length (L) were obtained from the slope of the regression lines and the inverse of y-intercept, respectively. In order to remove the contribution of instrumental broadening $[\Delta(2\theta)_{\mathrm{I}}]$, I adopted Warren's method (Warren, 1941) which is given by the following:

$$[\Delta(2\theta)]^2 = [\Delta(2\theta)_{\mathrm{M}}]^2 - [\Delta(2\theta)_{\mathrm{I}}]^2$$

where $[\Delta(2\theta)_{\mathrm{M}}]$ is the measured FWHM of the diffraction peak. The instrumental broadening was estimated by the Caglioti function using the diffraction pattern of powdered silicon wafer with adequate grain size, measured under the same geometrical conditions.

The prisms were pretreated with a sodium hypochlorite (NaClO) solution until individual calcite prisms separated from one another, then ground gently into powder in an alumina mortar. The powdered prisms were examined three times to estimate the error of measurements.

2A.4 Results

2A.4.1 Nanoindentation

Figure 2–7 shows the SEM images of the impressions on the calcite (001) surfaces formed by the nanoindentation experiments. The linear and curved cracks were found around the impression of Iceland spar (Figure 2–7a). Since the linear cracks develop triad-symmetrically and the load was applied on the (001) faces, they must correspond

to the {104} cleavage planes of calcite, indicating the mechanical weakness of abiogenic single-crystalline calcite. In contrast, the cracks did not develop widely and the cleavages were only partly observed around the impression of the prisms in

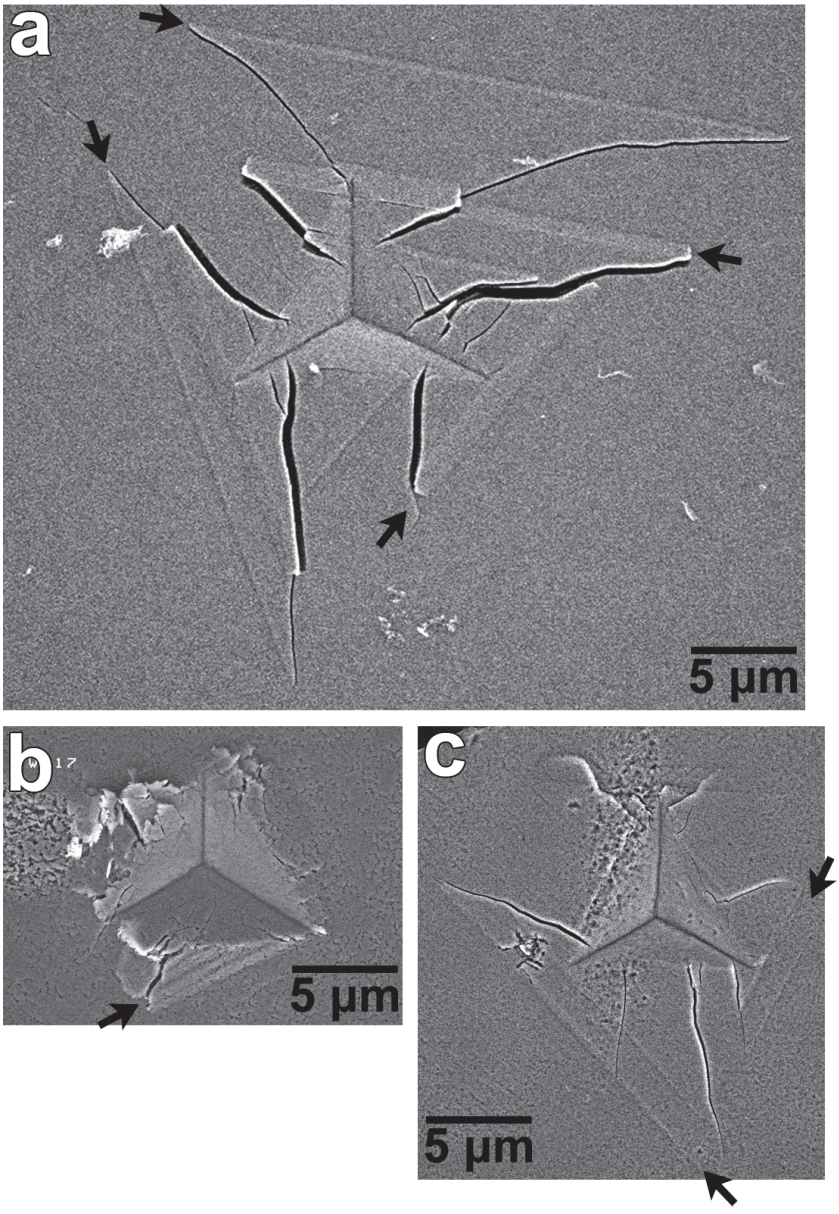

Figure 2–7. SEM images of the impressions formed by nanoindentation tests. (a) Iceland spar. (b) The prisms of *Pinctada*. (c) The prisms of *Atrina*. Arrows indicate cleavages along {104} planes of calcite.

Pinctada (Figure 2–7b). In the case of the prisms in *Atrina*, the cracks and cleavages along {104} planes around the impression are larger than *Pinctada*, and similar to Iceland spar (Figure 2–7c). Thus the prisms of *Pinctada* have a capacity for resisting cracks and cleavages, whereas those of *Atrina* have a character resembling abiogenic calcite crystals.

2A.4.2 TEM observation

Figure 2–8 shows TEM images of the calcite prisms in *Pinctada* and *Atrina*. The bright-field (BF) image of *Pinctada* captured under a strong diffraction condition exhibits complex jagged contrast which indicates the existence of sub-grain boundaries accompanying lattice strain (Figure 2–8a). In the case of *Atrina*, the prisms show not jagged contrast but smooth dark lines called bend contours in the BF image (Figure 2–8d). The smooth character of the bend contours means that the crystal is a monolithic single crystal. When the prisms were observed under a weak diffraction condition and with under-focus ($\Delta f \approx 2.3$ μm), many bright contrasts, which are considered to be intracrystalline OMs, appeared inside the crystals (Figure 2–8b and 2–8e). Since the bright contrasts became dark with over-focus, they are well-known Fresnel contrasts which correspond to materials with a lower electrostatic potential than the surrounding crystals. In the under-focused image, the intracrystalline OMs in *Pinctada* are distributed inhomogeneously and locally make striated forms (Figure 2–8b). The sub-grain boundaries in Figure 2–8a are formed at aligned intracrystalline OMs, suggesting that the inhomogeneous distribution of the intracrystalline OMs induces the sub-grain boundaries in the prisms of *Pinctada*. Since the *c*-axis of calcite is the top-left

direction of the image according to the diffraction pattern (Figure 2–8c), intracrystalline OMs are striated in a direction roughly perpendicular to the *c*-axis, in other words, parallel to the shell surfaces. Many bright Fresnel contrasts as intracrystalline OMs were also observed in the prisms of *Atrina* in the under-focused BF image in spite of their

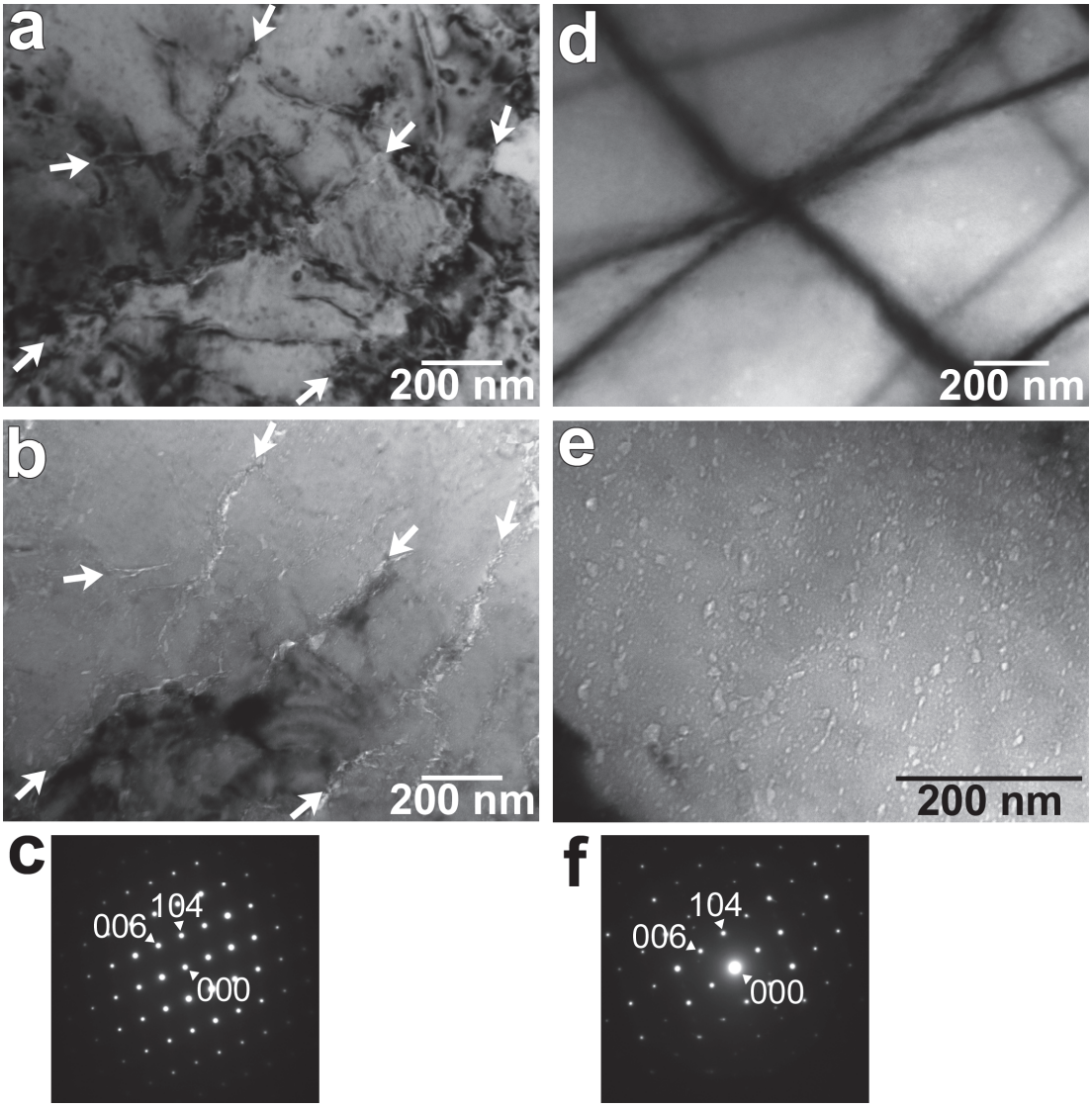

Figure 2–8. TEM images of the prisms of *Pinctada* (a–c) and *Atrina* (d–f). (a, d) BF images with strong diffraction contrast. (b, e) Under-focused BF images. Arrows indicate the locations of small-angle misorientation and aligned OMs. (c, f) Diffraction patterns obtained from the areas of (a) and (d), respectively.

single-crystalline feature, and they are distributed homogeneously (Figure 2–8e). Considering the *c*-axis is the top-left direction of the image as shown by the diffraction pattern (Figure 2–8f), the OMs of *Atrina* do not have distinctive shapes and distribution like those of *Pinctada*.

2A.4.3 STEM–EELS analysis

The Fresnel contrasts were confirmed to correspond to intracrystalline OMs using EELS analysis. The peak at 284 eV in the fine structure of carbon K-edge in EELS spectra arises from the electron transition from 1s to π^* bonds for carbon, indicating the existence of organic matter, graphite, amorphous carbon, etc., but never carbonate ions (Martin et al., 1989, 1996; Varlot et al., 1997, 1999; Mansot et al., 2003). Therefore this peak reflects the existence of organic matter in the investigated specimens. I used an EELS detector attached to a STEM, which enables us to acquire HAADF–STEM images and EELS spectra simultaneously. Figure 2–9a and 2–9b shows the HAADF–STEM images of the prisms of *Pinctada* and *Atrina*, respectively. The bright Fresnel contrasts in the under-focused TEM images were observed as dark contrasts in the HAADF–STEM images, indicating that these contrasts correspond to materials with lighter atoms. I acquired the EELS spectra from the dark contrasts (Figure 2–9c from 2–9a, 2–9d from 2–9b). Since both calcium carbonate crystals and organic matter are sensitive to electron beam irradiation, they are easily destroyed and degraded during the analyses (Varlot et al., 1997). To avoid the irradiation damage as much as possible, each spectrum was collected within 5 seconds. The spectra in the figure were obtained by integrating approximately 30 spectra in order to improve the signal-to-noise ratio. In

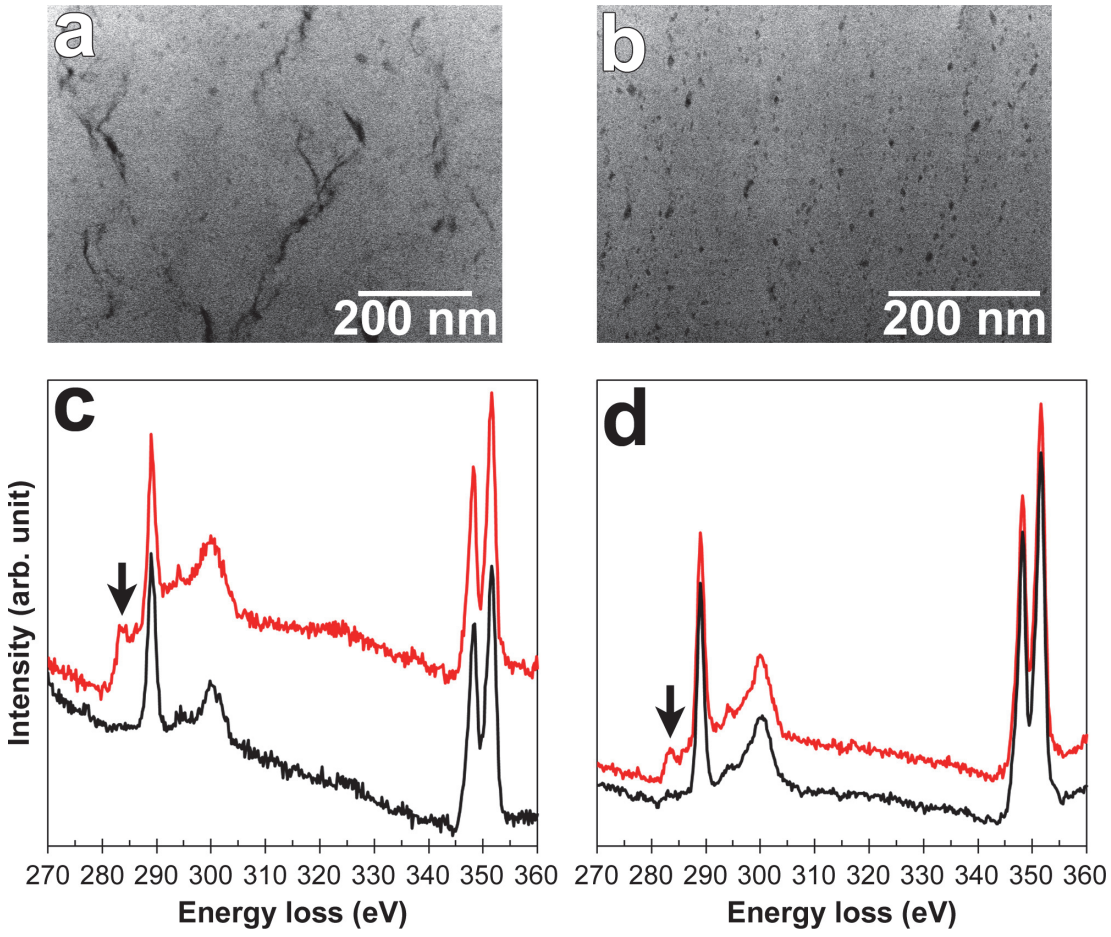

Figure 2–9. HAADF–STEM images of the prisms of *Pinctada* (a) and *Atrina* (b). EELS spectra obtained from the prisms of *Pinctada* (c) and *Atrina* (d). Red spectra from the dark contrasts in HAADF–STEM images, or the Fresnel contrasts in TEM images. Black spectra from only calcite crystals. Arrows indicate the 284 eV peaks.

each sample, the spectra from the Fresnel contrasts were opposed to those from areas of only calcite crystals without the low-Z contrasts. Compared with the spectra from only crystals (black lines), those from the low-Z contrasts (red ones) show the 284 eV peak, indicating that the low-Z contrasts, or the Fresnel ones, correspond to intracrystalline OMs. Note that the organic phases in the crystals can be recognized by the existence of the peak at 284 eV even though they have been already degraded owing to the

irradiation damage. Instead, we cannot know exactly what kinds of carbon species the OMs contain. The peaks around 347 and 350 eV are calcium $L_{2,3}$-edges, corresponding to the electron transitions from $2p_{1/2}$ to 3d and from $2p_{3/2}$ to 3d, respectively.

2A.4.4 XRD analysis

The Williamson–Hall plots obtained from XRD patterns of *Pinctada* and *Atrina* are shown in Figure 2–10. In the plots, steeper regression lines and larger y-intercept indicate more local lattice strain and smaller coherence length, respectively. Since the crystallographic properties of calcite are expected to be anisotropic, I analyzed the crystallinity along the *c*-axis and a_i-axes (i = 1–3) separately. The reflections that can be used for the direction along the *c*-axis are 006 and 00.12 (Figure 2–10a). In the case of the direction along the a_i-axes, 110 and 220 were selected (Figure 2–10b). The slopes of regression lines are considerably steeper for *Pinctada* than *Atrina*, and steeper along the *c*-axis than a_i-axes, indicating that the prisms of *Pinctada* have more local lattice strain than those of *Atrina*, and along the *c*-axis than a_i-axes. The larger local lattice strain in *Pinctada* is probably originated from the defective structure with the sub-grain boundaries observed by TEM, indicating that the defective structure is the character of whole calcite crystals in *Pinctada*. The strain-free feature of *Atrina* was reported also by Berman et al. (1993a) from the analysis of the XRD peak profiles. The coherence length is calculated from the Williamson-Hall plots by dividing the values of y-intercept by 0.94. When the y-intercept is 0.0005 $Å^{-1}$, the coherence length is approximately 200 nm (Figure 2–10c), which corresponds to the sizes of sub-grains in *Pinctada* in TEM images (Figure 2–8a). However, the coherence length varies considerably in the range

less than 0.0005 $Å^{-1}$ of y-intercept, therefore accurate coherence length was not obtained considering the errors of XRD measurements. In addition, the limit for estimating the coherence length from the peak width is approximately 100 nm, because the coherence length more than 100 nm does not affect the peak width in XRD profiles. All of the y-intercept is smaller than 0.001 $Å^{-1}$, which corresponds to the coherence length of 94 nm. Hence, the coherence length of the prisms is larger than 94 nm for both

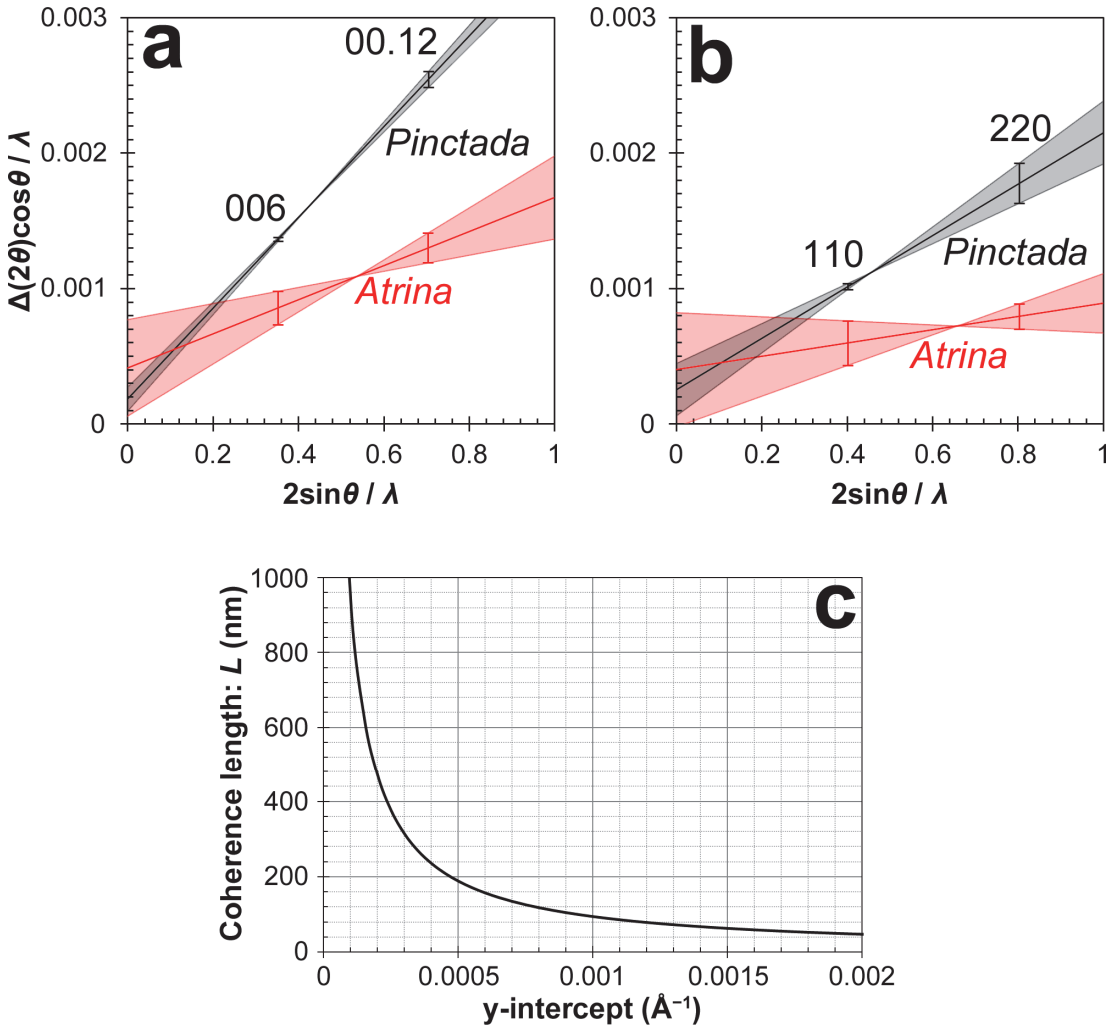

Figure 2–10. Williamson–Hall plots of the prisms of *Pinctada* and *Atrina* for the 006 and 00.12 (a), 110 and 220 (b) peaks in XRD profiles. (c) Coherence length as a function of the y-intercept of Williamson–Hall plots.